



UNIVERSIDAD  
**NACIONAL**  
DE COLOMBIA

# **Design of scaffolds for bone tissue regeneration through diagnostic imaging and generative design**

**Fahir Dario Castañeda Parra**

Universidad Nacional de Colombia Sede Bogotá  
Facultad de Ingeniería, Departamento de Ingeniería Mecánica y Mecatrónica  
Bogotá, Colombia

2023

# **Design of scaffolds for bone tissue regeneration through diagnostic imaging and generative design**

Fahir Dario Castañeda Parra

Thesis in partial fulfillment of  
the requirements for the degree of:  
Master's in engineering - Materials and Processes

Director:

Diego Alexander Garzón Alvarado

Codirector:

Marco Antonio Velasco Peña

Investigación Line:

Tissue Engineering

Universidad Nacional de Colombia Sede Bogotá  
Facultad de Ingeniería, Departamento de Ingeniería Mecánica y Mecatrónica  
Bogotá, Colombia

2023

## Acknowledgments

I want to thank all people who helped me during each step of this journey.

I especially want to thank whom I consider my two mentors and the directors of this thesis, professor Diego Alexander Garzón Alvarado and professor Marco Antonio Velasco Peña, for all their advice and guidance in the research.

I also want to thank my aunt Claudia for allowing me to explore other research fields beyond the commons of my profession.

To my mother, Monica, for always being there for me and for always having an open hand and a kind heart ready to help and guide me through difficult times.

To my family for all their support in my creative work.

To my love and best friend, Laura, for her support, time, and inspiration no matter the day.

Finally, to all the people who one way or another have known me and worked with me.

## Abstract

### **Design of scaffolds for bone tissue regeneration through diagnostic imaging and generative design**

Bone tissue engineering focuses, in addition to other things, on the understanding of bone structures to promote their formation with scaffolds. The manufacturing processes of scaffolds with variable density are complicated for traditional manufacturing methods, where localized holes are drilled in structures to mimic bone architecture. In recent years, tissue engineering has benefited from advances in the development of additive manufacturing, which allows the creation of complex geometries such as scaffolds. To explore this method, the use of image-based design is proposed. In this thesis, a scaffold with variable internal density is developed, which can be fabricated by additive manufacturing by controlling the external and internal geometry of the structure, porosity, and pore size from diagnostic images.

**Key words:** cellular materials; generative design; finite element method; bone scaffold.

## Resumen

### **Diseño de scaffolds para regeneración de tejido óseo mediante imágenes diagnósticas y diseño generativo**

La ingeniería de tejidos ósea se encarga, entre otros, de la comprensión de las estructuras de los huesos para tratar de promover su formación con scaffolds. Los procesos de fabricación de scaffolds con densidad variable se dificultan para métodos tradicionales de manufactura en donde se realizan agujeros localizados en estructuras con el objetivo de lograr imitar la arquitectura del hueso. En los últimos años, la Ingeniería de Tejidos se ha visto beneficiada de los avances que se han realizado en el desarrollo de la manufactura aditiva, la cual permite la creación de geometrías complejas como las de los scaffolds. Para incursionar en este método, se propone el uso del diseño basado en imágenes diagnósticas. En esta tesis se desarrolla un scaffold con densidad interna variable, que puede ser llevado a su fabricación por manufactura aditiva controlando geometría externa e interna de la estructura, porosidad y tamaño de poro a partir de imágenes diagnósticas.

**Palabras claves:** materiales celulares; diseño generativo; método de elementos finitos; andamio óseo.

## Table of Contents

Abstract .....	IV
Resumen .....	V
Figure list .....	VII
Table list .....	X
Introduction.....	1
1. Background.....	4
1.1. Design of the internal structure and porosity.....	4
1.2. Design of the algorithm for the internal architecture.....	5
1.2.1. Overview of the proposed algorithms.....	5
1.2.1.1. Cellular structures from a cloud of points.....	5
1.2.1.2. Cellular structures from a uniform trabecula .....	9
1.2.2. Illustrative examples and mechanical behavior.....	13
1.2.2.1. Application in the interpretation of trabeculae in bones .....	13
1.2.2.2. Model validation by FEA .....	17
1.2.2.3. Experimental model validation .....	19
2. Proposed algorithm for the design of scaffolds for bone tissue regeneration using diagnostic images.....	24
2.1. Parameters for the design of 3-D scaffolds.....	24
2.2. Code generation.....	25
2.2.1. Adapting the algorithm with Voronoi to 3D .....	25
3. Application of the algorithm in the interpretation of bone.....	34
3.1. FEA Simulations.....	34
3.2. Results.....	43
3.2.1. Apparent Young's Modulus .....	43
3.2.2. Compression test.....	50
4. Discussion .....	54
5. Conclusions .....	55
5.1. Products.....	56
5.2. Future work.....	56
References .....	57

## Figure list

	<b>Page</b>
Fig. 1 Contour generation. From left to right: Base image, alpha layer obtained from the image and external contour obtained.....	6
Fig. 2 Cloud of points generated within the domain. ....	6
Fig. 3 Voronoi diagram (left) and Delaunay triangulation obtained from the point cloud.....	6
Fig. 4 Initial skeleton and its transition to a porous solid structure. ....	7
Fig. 5 Final result of the Voronoi and Delaunay algorithms.....	7
Fig. 6 Algorithm for the generation of a solid with pores in Voronoi.....	8
Fig. 7 Algorithm for the generation of solids with pores in Delaunay.....	8
Fig. 8 Square surface generated by the algorithm. ....	9
Fig. 9 Generation of structures with equilateral triangles. In the upper part, the three triangular meshes that are used to obtain points in an organized way, as used in this example, are shown. In the lower part, there are three randomly generated point clouds and a cloud of points generated in the contour for the management of the Delaunay algorithm. ....	9
Fig. 10 Clouds of points filtered by the density value $\rho_i$ of the image; each cloud obtains a range of density values on which to work.....	10
Fig. 11 Final cloud of points obtained from the final union of the previous three. On the left is the random cloud of points; on the right is the organized cloud of points from the equilateral triangle meshes. ....	10
Fig. 12 Voronoi diagram and Delaunay mesh obtained using the random point cloud; triangular mesh obtained using the final cloud of points. ....	11
Fig. 13 Final result of the algorithms with uniform trabeculae of Voronoi and Delaunay, as well as the algorithm of uniform trabeculae with equilateral triangles. ....	11
Fig. 14 Algorithm for the generation of a Voronoi solid with uniform trabeculae. ....	12
Fig. 15 Algorithm for the generation of a Delaunay solid with uniform trabeculae. ....	12
Fig. 16 Algorithm for the generation of a Voronoi solid with uniform trabeculae. ....	13
Fig. 17 Left: Radiography of the femoral head used for the example of the method. Center: Alpha layer of the radiography. Right: Outline obtained. ....	14
Fig. 18 Results obtained from the random point cloud (left) and the organized point cloud (right). ...	14
Fig. 19 CAD models obtained from the application of the method by regular algorithms. From left to right: regular Voronoi, regular Delaunay and regular triangular mesh.....	15
Fig. 20 Additive manufacturing results of CAD models derived from radiography. ....	16

Fig. 21 Results on the possibility of iteration of the method: Voronoi with 581 pores, Voronoi with 1266 pores, increasing the thickness of internal trabeculae and increasing the thickness of the external wall. ....	16
Fig. 22 Porosity values for the results obtained from the application of the algorithm of regular trabeculae as presented in [42]. ....	17
Fig. 23 Boundary conditions for the optimization algorithm as presented in [42]. ....	18
Fig. 24 Results obtained from the TO algorithm for different volume fractions: 40%, 60%, and 80%, as presented in [42]. ....	18
Fig. 25 Displacement fields in specimens using frame elements as presented in [42]. ....	19
Fig. 26 3D-printed structures with Delaunay, Voronoi and equilateral triangles for fraction volumes of 80%, 60% and 40%, as presented in [42]. ....	20
Fig. 27 Force (kgf) vs. displacement (mm) for all the tested specimens [42]. ....	21
Fig. 28 Failure of the Delaunay cellular structures with fraction volumes: 80%, 60% and 40% [42]. ....	22
Fig. 29 Failure of the Voronoi cellular structures with fraction volumes: 80%, 60% and 40% [42]. ....	22
Fig. 30 Failure of the triangular cellular structures with fraction volumes: 80%, 60% and 40% [42]. ....	23
Fig. 31 The white curves form the general external geometry of the bone. ....	25
Fig. 32 The contours are located on the z-axis forming the topographic lines that describe the external architecture of the bone. ....	26
Fig. 33 Solid surface created from the topographic lines. ....	26
Fig. 34 The two point clouds generated within the contours of the bone are shown. ....	27
Fig. 35 The generated Voronoi diagram is placed inside a bounding box with the minimum dimensions corresponding to those of the bone. ....	28
Fig. 36 Outer surface of the bone, generated after the Boolean operation. ....	29
Fig. 37 Axial and sagittal cross-sections demonstrating the internal architecture of the bone generated using the established trabeculae width. ....	30
Fig. 38 Additive manufacturing result of the CAD model derived from the diagnostic images. ....	31
Fig. 39 Three slices at different heights of the Z-axis of the generated structure and their relation to CT scans at the same height in the bone are presented. ....	31
Fig. 40 The relation of the low and high material density zones concerning their counterparts in the generated porous structure. ....	32
Fig. 41 Algorithm for the generation of a porous solid from diagnostic images. ....	32
Fig. 42 Algorithm for the generation of a porous solid from diagnostic images as implemented in Grasshopper. ....	33
Fig. 43 Pig bone scaffold, with its main faces in the X, Y, and Z axes. ....	34



Fig. 44 The blue cube is the 5 mm cube within the body of the human vertebra to be used for the finite element analysis. ....	35
Fig. 45 Each cell in the cellular structure contains a sphere to measure the nominal pore size. ....	38
Fig. 46 Histograms showing the distribution of pore sizes for the different structures generated. ....	40
Fig. 47 Solid cube manufactured using SLA, the top face and one of the lateral faces can be appreciated, and the images were obtained using a stereomicroscope. ....	40
Fig. 48 side view showing the boundary conditions for the compression test. ....	41
Fig. 49 Methodology to obtain the apparent Young's modulus of a porous solid. ....	41
Fig. 50 Tabulated data showing iterations, stress value, % change and elements as presented in the worksheet by the software. ....	42
Fig. 51 Geometric model of the pig bone scaffold imported to Ansys. ....	43
Fig. 52 Constraints and displacements for each axis. The green arrow represents the main direction of the applied displacement. ....	43
Fig. 53 Deformation results for the different displacements applied. ....	44
Fig. 54 The correlation of the porosity percentage with the apparent Young's modulus of the structure is shown. ....	50
Fig. 55 3D printed structures for each trabecula thickness selected and the pig bone scan. ....	51
Fig. 56 Shimadzu UW620H precision balance and Nikon SMZ800 stereo microscope were used for the dimensional analysis. ....	51
Fig. 57 Compression test setup for each specimen. ....	52
Fig. 58 The correlation of the porosity percentage with the Young's modulus of the specimens is shown. ....	53
Fig. 59 possible surface roughness proposed. ....	56

## Table list

	<b>Page</b>
Table 1 Scaffolds with a variety of trabecular widths .....	36
Table 2 Number of pores in each structure and size range .....	38
Table 3 Material properties obtained after characterization of the cube. ....	40
Table 4 Porosity and apparent Young's Modulus for the pig bone .....	44
Table 5 Deformation results for the different displacements applied for each of the corresponding trabeculae thicknesses. ....	44
Table 6 Porosity and apparent Young's Modulus for the structures generated with the proposed algorithm increasing by 0.1 mm and alternating in the XYZ axis.....	47
Table 7 Porosity and apparent Young's Modulus for the annexed structures generated with the proposed algorithm, increasing by 0.01 mm, 0.001 mm, and alternating in each axis. ....	48
Table 8 Results of the selected structures whose values are close to those found in pig bone.....	49
Table 9 Results of the compression test for the selected manufactured specimens.....	52

## Introduction

Bone tissue can be damaged for different reasons, including external mechanical factors such as accidents or pathological lesions due to diseases related to bone tissue deficiency, such as orthogenesis imperfecta, osteoporosis, osteomalacia, osteomyelitis, and cancer, among others [1]. Bone is the central component of the musculoskeletal system, a complex, calcified connective tissue that protects vital organs, supports the body's mobility, stores calcium and other minerals, and generates mesenchymal and hematopoietic stem cells [2].

Although the bones of the human body have some self-regenerating properties, there are conditions in which these properties are insufficient to restore damaged tissue [3]. This is the case for comminuted fractures or significant bone defects, where the body does not have the capacity to follow normal repair processes by ossification. Every year, 8.6 million surgical interventions are performed worldwide to treat this type of fracture with the placement of an implant [4]. Only in Colombia in 2012 were approximately 2,609,858 men and 1,423,559 women over 50 living with osteopenia and osteoporosis, respectively. It is projected that the numbers will increase by 2020, and in 2050, the numbers could reach up to 3'852,200 in the case of osteopenia and 2'101,000 in the case of osteoporosis [5]. Similarly, in 2009, Colombia performed approximately 10,000 knee and hip implants each year. However, most cases occur in adults over 60 years of age. In recent years, there has been a need to perform these procedures in people in their 40 s, as well as in young people with sports injuries and motorcycle accidents and in children who have suffered hip dysplasia or trauma to joints such as the knee [6], [7].

Currently, the development of medicine and research has provided several solutions, such as implants; however, these have several complications, such as the generation of diseases and the need for several surgical interventions [8]. On the other hand, tissue engineering offers another solution based on the possibility that the regeneration of new tissue can be guided through the combination of cells, biomaterials, and bioactive molecules. This principle, called the tissue engineering triad, comprises stem cells, growth factors, and three-dimensional scaffolds or scaffolds [9]. The scaffold is a cellular material whose primary function is to support the adhesion, proliferation, and migration of cells, as well as their differentiation and maturation into an osteoblast phenotype [10].

Cellular materials offer unique functional characteristics, such as high specific strength and stiffness, mechanical energy absorption, and heat transfer control [11]. These materials are formed by periodic or stochastic arrangements of cells and can have configurations in two dimensions such as honeycombs or three dimensions in arrangements of polyhedrons [12]. In nature, cellular materials contain varying densities depending on the needs of the tissue, organ, or organism [13].

Bones are a cellular material generally with a variable internal density because the epiphyses of long bones have trabecular bone in their interior, which may contain a higher density in locations with a greater mechanical load [14], [15].

The design and manufacture of cellular materials for bone tissue regeneration have the following design requirements [16]–[20]: control of the product architecture at different levels, from the external shape to the internal structure, with an optimized pore geometry, since the structures must be highly porous and have pore sizes greater than 400  $\mu\text{m}$ ; their mechanical properties must be appropriate to support the loads and their elastic modulus must be similar to that of bone to reduce load transfer and thus avoid failure; and they must be biocompatible and biodegradable to ensure cell survival and guarantee adequate degradation time to allow bone tissue remodeling. These variables are important factors for cell adhesion and proliferation processes and for meeting other clinical requirements [1]. The mechanical performance of cellular materials depends on factors such as cell topology; cell number; geometric parameters, including trabeculae diameter and cell size; material and manufacturing process; and structural limits and loading conditions [21], [22].

Among the methods to be considered for the generation of the scaffold geometry, we can find the additive manufacturing process (SLA, SLS, FDM), the design by mechanical loads from load analysis for topological optimization (TO), the Computer-Aided Design (CAD) based on constructive solid geometry modeling tools (CSG) or triple periodic minimum surfaces (TPMS) and the design based on diagnostic images [1], [23]. CSG uses polyhedra as unit cells, which generate a repeating pattern extending in multiple directions. [24], [25]. On the other hand, TPMSs are surfaces with a zero-mean curvature [26], and they differ from the previous ones because they have a higher area/volume ratio and can have size gradients in one direction [27]. Topological optimization is a method that distributes the material within a given space for a set of loads, boundary conditions, and constraints to maximize or minimize the system response for a given function [28]. Finally, diagnostic imaging presents an alternative method for designing and manufacturing bioinspired scaffolds, which in their micro- or mesostructure resemble the structures in bone tissue [29].

Of the methods presented above, CSG and TPMS, although widely used, have difficulties because they form symmetry groups with a uniform distribution, which makes it challenging to create regions with variable properties within the structure, as well as their adaptation to organic structures. On the other hand, the results of mathematical topological optimization methods are generally represented by raster images in grayscale, where the pixels are not primitive design entities that can be easily represented and parameterized in CAD programs.

On the other hand, the method based on diagnostic images would allow the design of scaffolds for specific patients and sites with controlled internal architecture. The scaffold topology is designed using image processing techniques and then converted to data used to construct generative design tools, in which algorithms and rules programmed by code are used to configure the scaffold or its mold [23], [30]–[32]. With this in mind, this thesis aims to make an algorithm that generates a 3D porous structure that considers the different parameters found in the literature for the scaffold design parameters. To fulfill this goal, the following specific objectives have been proposed:

- Define the input and output variables to be used by the algorithm for the design of a scaffold.
- Program the algorithm using generative design CAD tools.
- Characterize the compression mechanical behavior of the generated structures through finite element analysis and mechanical testing of specimens manufactured by additive manufacturing.

The development of this thesis is as follows. Chapter 1 corresponds to the background that this thesis will take into account as a starting point for the research. Chapter 2 describes a methodology for designing scaffolds for bone tissue regeneration using CT scans. In Chapter 3, the computer simulation of a compression test from a representative volume of a scaffold taken from a vertebra is presented. This simulation is later validated through experimental compression tests.

# 1. Background

The present research took as a reference the conclusions of four previous investigations, the first three taken from the literature review and the last one where an investigation was carried out during my industrial design undergraduate thesis and later continued in collaboration with the GNUM research group at the National University of Colombia. For the presentation of this last reference, the investigation carried out will be presented, as well as some of the algorithms generated along it.

## 1.1. Design of the internal structure and porosity

- G. Marchiori and his collaborators (2019) designed a method for optimizing scaffold design. First, they used a CAD method to draw the scaffold architectures and calculate their porosities. Then, they used the Taguchi method to select the main combinations of scaffold architecture and generic material. Finally, by using finite element analysis, they simulated the mechanical properties of each of the chosen combinations, and the results were used to generate a regression model to determine the effect of the combinations of different architectures and materials on the mechanical performance of the scaffolds. It is concluded that this method can become expensive and lengthy when testing multiple design iterations and many structures [33].
- A. Di Luca and his colleagues (2016) present a study in which they aim to generate scaffolds manufactured by additive manufacturing that simulate the radial porosity gradient found in long bones due to the differences between cortical bone and trabecular bone. Additionally, the behavior of stromal stem cells (hMSCs) was evaluated to observe how the scaffold architecture influences the osteogenic differentiation of the cells. It is concluded that cells residing in different areas of the gradient demonstrated a tendency toward osteogenic differentiation due to pore size due to greater nutrient and oxygen supply in compartments with wider pores. It is suggested that pore size gradients be taken into consideration as an important structural factor in scaffold design [34].
- G. Staffa and colleagues (2010) described a method for cranioplasty using a custom-made, premanufactured, biomimetic, biocompatible, and osteoconductive 3D prosthesis made of porous hydroxyapatite. The prosthesis was manufactured under European standards. Fifty-one patients with defects in fronto-parietal, fronto-temporal, and fronto-occipital areas were treated. Computed tomography scans of the defects were used to produce 1:1 models of the skull, and the prosthesis was finally manufactured based on the model and obtained images. The personalized scaffolds were adapted to the morphology of the defect without generating mechanical complications, and the clinical data demonstrate good performance in the reconstruction of the defects, allowing for cell implantation and vascularization [35].

## 1.2. Design of the algorithm for the internal architecture.

My undergraduate thesis in Industrial Design is an important precedent for the current project, as it dealt with a similar topic and provided valuable insights into the design process of an efficient and novel framework (algorithm) to obtain cellular structures with variable pore density within the domain, which can be brought to its fabrication by additive manufacturing, without relying on a given periodic cellular structure.

The methodology was tested on grayscale images from X-ray and topological optimization algorithms to obtain CAD models suitable for additive manufacturing. These models were subsequently manufactured through an additive manufacturing process. The results show that the developed tool is able to successfully obtain cellular structures; moreover, the 3D printed specimens were evaluated through both FEM and physical tests to compare which of the trabeculae shapes was better for loading transmission.

### 1.2.1. Overview of the proposed algorithms

In this section, we propose two generative design tool algorithms that, from grayscale images that represent a density field, determine the formation of the internal cellular structure using Voronoi diagrams or Delaunay triangulation. The first algorithm generates an initial cloud of points according to the intensity of colors (or grayscale) of the domain. The second algorithm establishes the initial distribution of points from different density meshes. The tools were implemented in the Grasshopper program (McNeel, USA). Grasshopper is an algorithm editor that is integrated into the modeling software Rhinoceros 3D Version 6 (McNeel, USA).

#### 1.2.1.1. Cellular structures from a cloud of points

The first group of proposed algorithms aims to build a porous structure from a cloud of points distributed as a function of the intensity of the grayscale within a geometry. The quantity of points in the domain can be controlled as needed.

**Step 1- contour of the domain:** In the first step, the algorithm creates the external contour of the figure. This is achieved through a sampling process in Grasshopper, which extracts information from the alpha channel of the image. This channel corresponds to the opacity (i.e., transparency) of each pixel and is one of the four channels in which an RGBA image can be decomposed (the others being red, green, and blue) [36]. Thanks to the image-handling capabilities of the algorithm, the order and number of colors in the image are not important, as the algorithm always obtains the external contour. Using this information, the algorithm draws the contour and extracts the external geometry (Fig. 1); note that the geometry shows greater intensity of gray toward its contour and lower intensity in the central part.

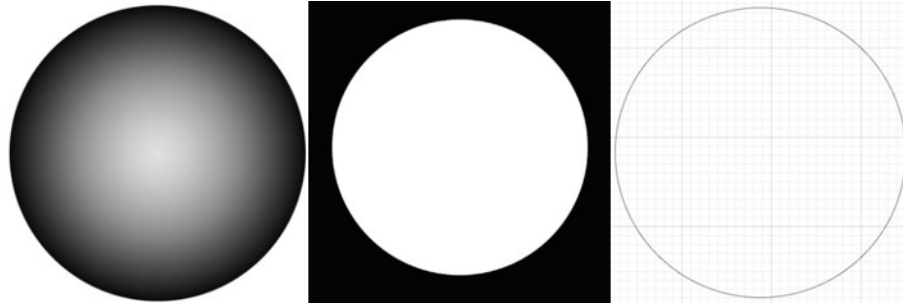


Fig. 1 Contour generation. From left to right: Base image, alpha layer obtained from the image and external contour obtained.

**Step 2 – distribution of seed points:** Points are distributed within the domain based on the grayscale of the image, with a distribution proportional to a value  $p_i$ . Grasshopper assigns a  $p_i$  value to each pixel of the image, with  $p_i = 1$  for absolute black and  $p_i = 0$  for absolute white. Areas of higher  $p_i$  intensity have a greater density of points, and each point adopts the  $p_i$  value of the closest pixel. The number of points and stochasticity of distribution can be controlled in Grasshopper (Fig. 2).

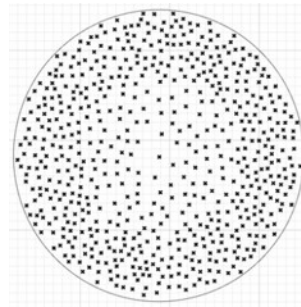


Fig. 2 Cloud of points generated within the domain.

**Step 3 – Drawing of the Voronoi diagrams and Delaunay triangulation:** The previously generated points can be used to draw either a Voronoi diagram or a Delaunay triangulation. In a Voronoi diagram, each point is the center of a polygon that divides the surface into closed polygons that coincide with adjacent polygons [37]. In a Delaunay triangulation, the points are the vertices of a network of triangles where no circumcircle contains any other vertex [38] (Fig. 3).

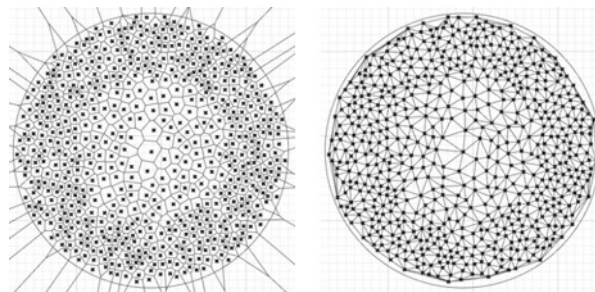


Fig. 3 Voronoi diagram (left) and Delaunay triangulation obtained from the point cloud.



**Step 4 – Scallation of the strut and Boolean operation:** The Voronoi polygons are scaled based on the value of  $p_i$  associated with the generating point. For Delaunay triangles, an extra point is calculated at the triangle center with a value  $p_i$  equal to the closest pixel. If the central point of a polygon has a value of 0, it will disappear (Fig. 4). The polygons are then used to remove material from a solid surface generated by the external outline of the geometry using a Boolean operation. The geometry's outline is used as the cutting edge, and excess lines are removed to clean the geometry (Fig. 5).

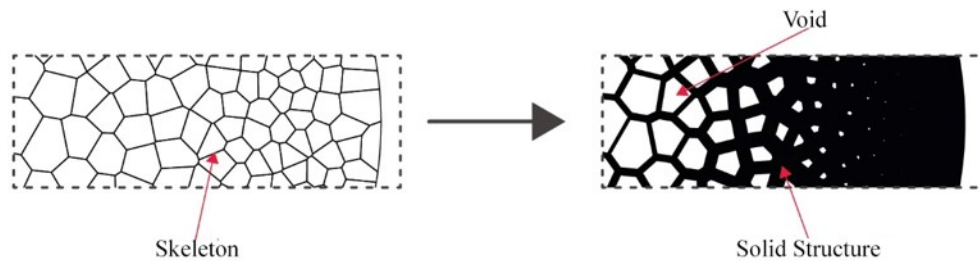


Fig. 4 Initial skeleton and its transition to a porous solid structure.

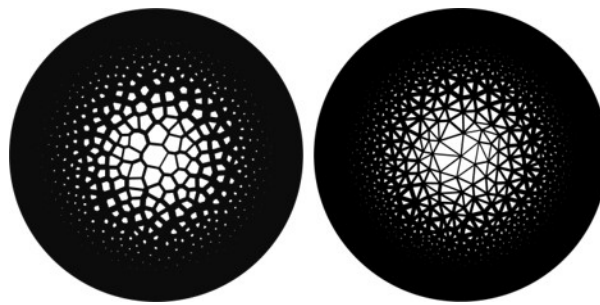


Fig. 5 Final result of the Voronoi and Delaunay algorithms

*Algorithms - Cellular structures from a cloud of points according to  $p_i$*

Fig. 6 and Fig. 7 present the algorithms developed for this methodology. Fig. 6 illustrates an algorithm that automatically constructs a porous structure from a cloud of points within the image contour, generating a customizable Voronoi diagram that allows for control of pore size and density. This algorithm results in a porous geometry that is ready for manufacturing, utilizing definitions implemented in Grasshopper and Rhinoceros 6.

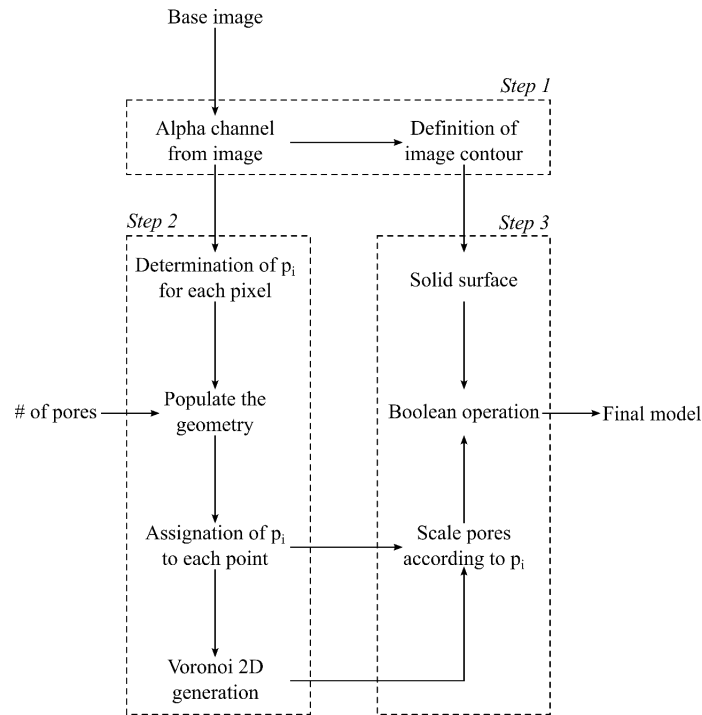


Fig. 6 Algorithm for the generation of a solid with pores in Voronoi.

The algorithm in Fig. 7 creates a solid with triangular pores arranged in a Delaunay mesh. This allows control over the number and size of the pores, and the final geometry is generated using Grasshopper definitions.

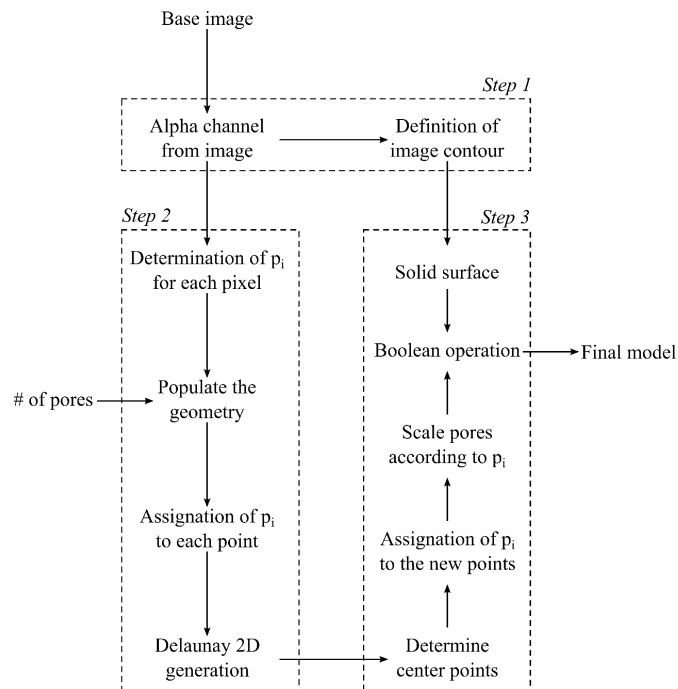


Fig. 7 Algorithm for the generation of solids with pores in Delaunay.

### 1.2.1.2. Cellular structures from a uniform trabecula

The second proposed algorithm can obtain a cellular structure with a uniform pore distance, calculated from polygons in Voronoi, Delaunay triangulation or equilateral triangles.

**Step 1 - contour of the domain:** The algorithm obtains the geometry contour from the image's alpha layer and generates a rectangular surface that encompasses the image's contour (Fig. 8).

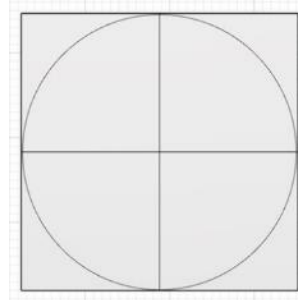


Fig. 8 Square surface generated by the algorithm.

**Step 2 - distribution of seed points:** The specific type of structure desired will determine the steps in this process. For equilateral structures, triangular meshes of different sizes and densities are created, with points extracted from each mesh (Fig. 9- top). For Voronoi or Delaunay structures, 3 clouds of points with varying densities are proposed (Fig. 9 - bottom). The number of elements in each mesh can be controlled, allowing for direct control over the total point density. However, it is important to consider that computational cost increases as the number of elements, points, meshes, or clouds increases.

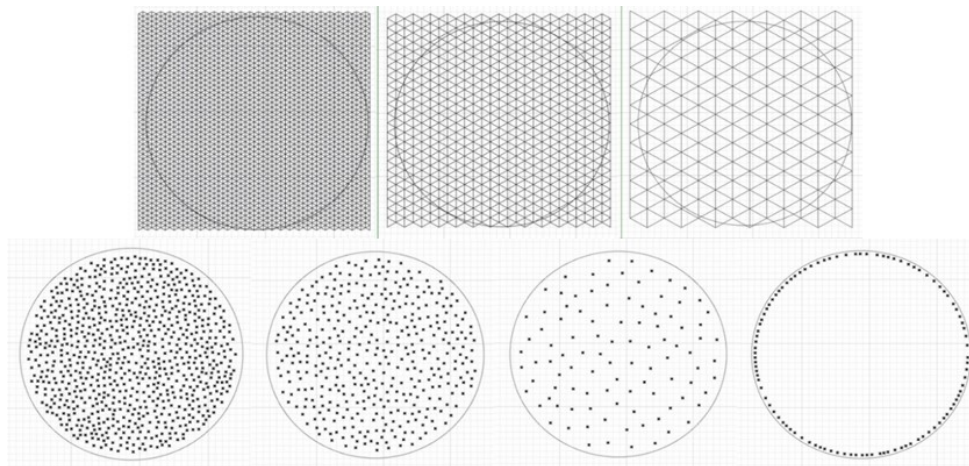


Fig. 9 Generation of structures with equilateral triangles. In the upper part, the three triangular meshes that are used to obtain points in an organized way, as used in this example, are shown. In the lower part, there are three randomly generated point clouds and a cloud of points generated in the contour for the management of the Delaunay algorithm.

**Step 3** – *elimination of points according to  $p_i$  & combination of clouds*: Gray intensity is assigned to each triangular mesh or point cloud ranging from  $p_i < 1$  to  $p_i = 1$  (Fig. 10), with higher values of  $p_i$  assigned to denser meshes or clouds. The resulting points are combined into a single cloud, with denser meshes given precedence in areas where multiple clouds coincide (Fig. 11).

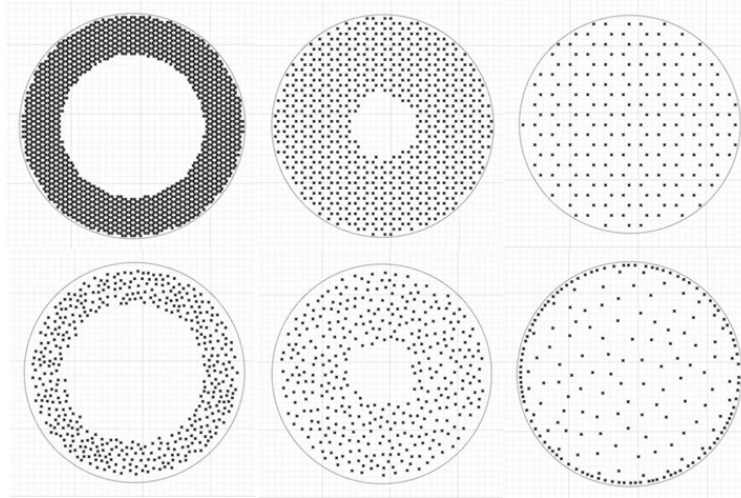


Fig. 10 Clouds of points filtered by the density value  $p_i$  of the image; each cloud obtains a range of density values on which to work.

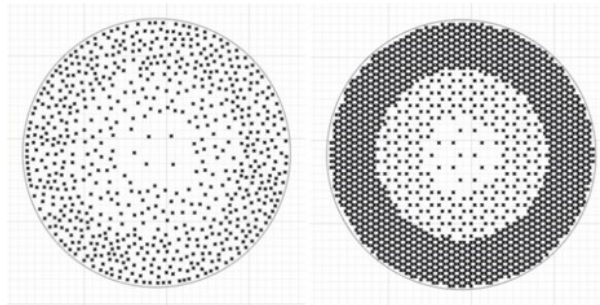


Fig. 11 Final cloud of points obtained from the final union of the previous three. On the left is the random cloud of points; on the right is the organized cloud of points from the equilateral triangle meshes.

**Step 4** – *drawing of the Voronoi diagrams and Delaunay triangulation*: The point cloud is used to create a structure of equilateral triangles or polygons in Voronoi or a Delaunay mesh. The distance between pores is user-controlled and uniform (Fig. 12).

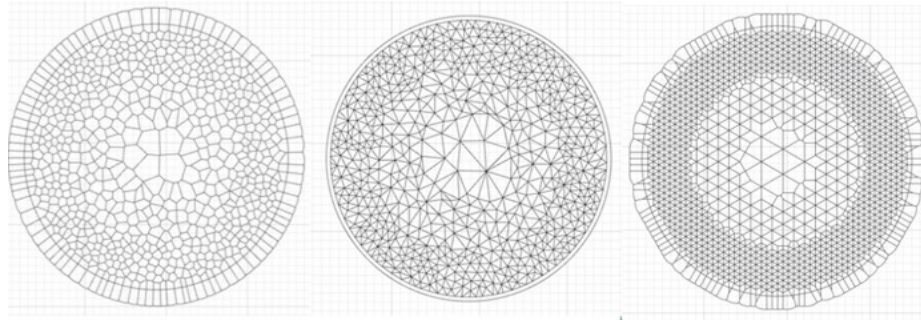


Fig. 12 Voronoi diagram and Delaunay mesh obtained using the random point cloud; triangular mesh obtained using the final cloud of points.

**Step 5 – Thickening of the strut:** The calculated contour delimits the internal geometry to obtain the final structure (Fig. 13). The thickness of the contour can be controlled if necessary.

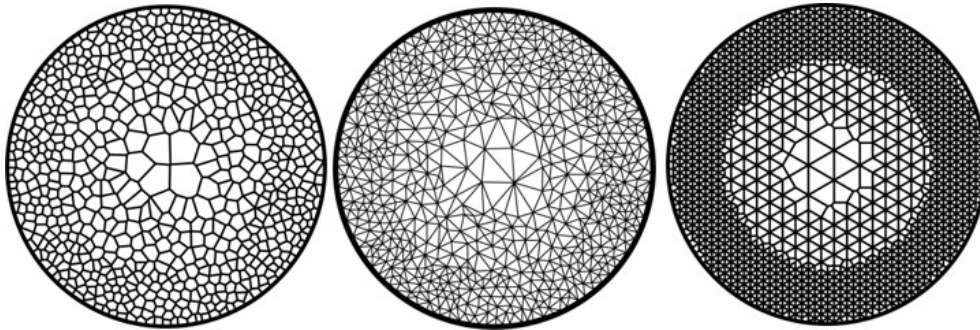


Fig. 13 Final result of the algorithms with uniform trabeculae of Voronoi and Delaunay, as well as the algorithm of uniform trabeculae with equilateral triangles.

#### Algorithms - Cellular structures from a cloud of points

The algorithms proposed in these methodologies are shown in Fig. 14, Fig. 15 and Fig. 16. The algorithm used to develop Voronoi's uniform trabeculae is shown in Fig. 14; Delaunay's uniform trabeculae algorithm is shown in Fig. 15; and finally, the algorithm and uniform trabeculae with equilateral triangles are shown in Fig. 16. For explanatory purposes, all algorithms are shown as if only 3 clouds of points or meshes are considered.

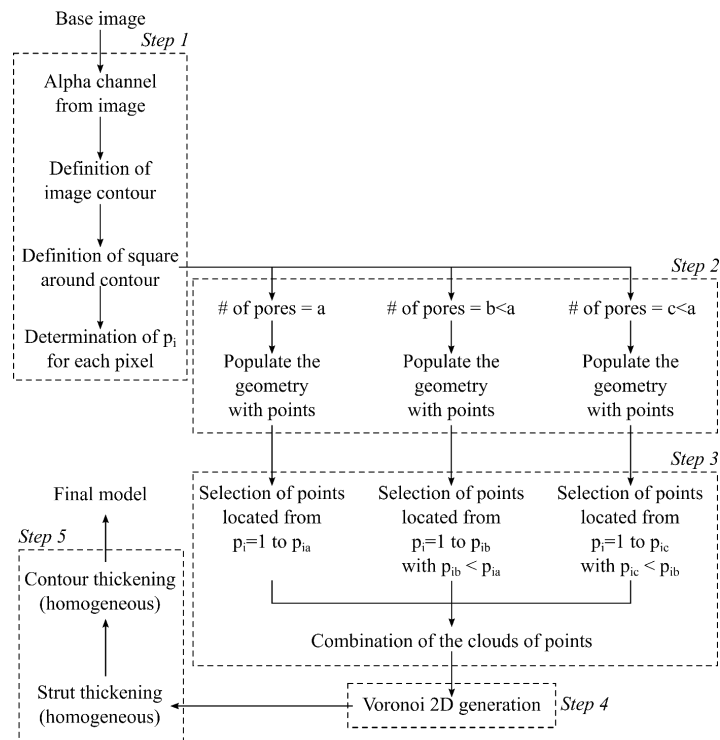


Fig. 14 Algorithm for the generation of a Voronoi solid with uniform trabeculae.

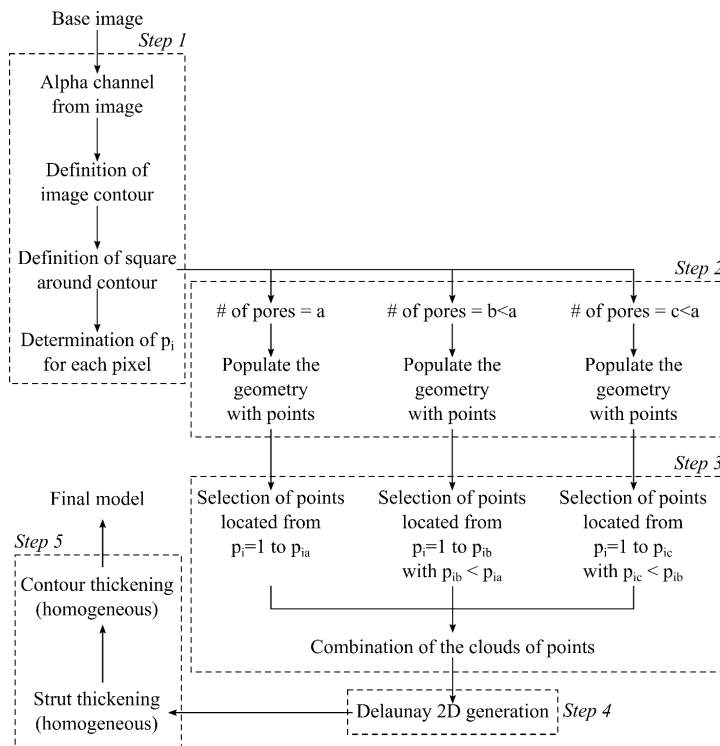


Fig. 15 Algorithm for the generation of a Delaunay solid with uniform trabeculae.

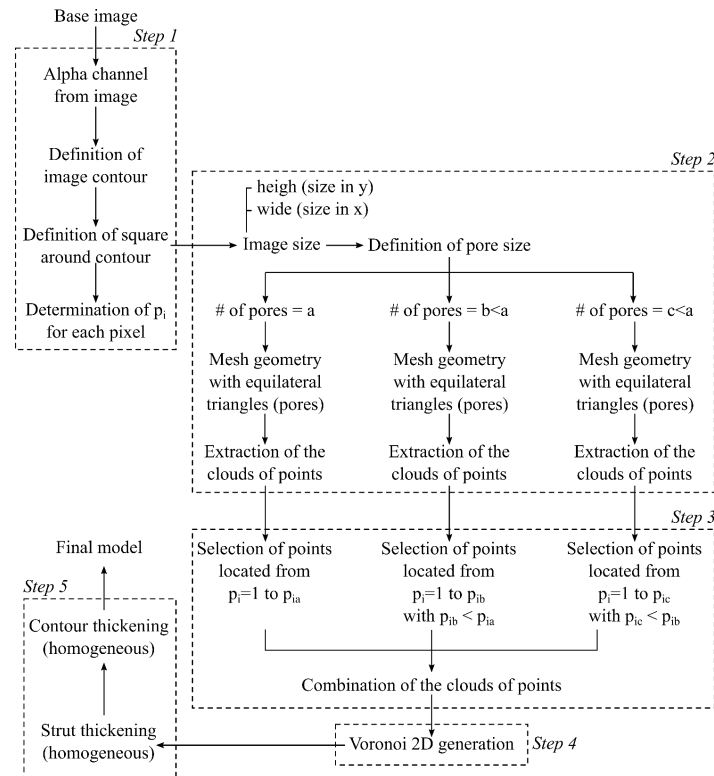


Fig. 16 Algorithm for the generation of a Voronoi solid with uniform trabeculae.

## 1.2.2. Illustrative examples and mechanical behavior

After the mentioned degree project, research was carried out within the GNUM research group at the National University of Colombia, in which the resulting algorithm was applied to a series of mechanical tests and applications to better describe the compressive mechanical behavior of the generated structures. The aim was to decide and characterize an internal structure for future work. The proposed algorithms will be applied to an X-ray of a human femur head, the result of a bone-remodeling algorithm, and the geometry obtained by topological optimization to test their feasibility.

### 1.2.2.1. Application in the interpretation of trabeculae in bones

The algorithm's ability to generate regular trabeculae for internal bone geometry is tested using diagnostic imaging such as radiographies and CT scans, which display the density of different bone types in grayscale [39] The test uses an X-ray of the proximal end of a femur (Fig. 17, left). and one of the proposed algorithms (1.2.1.2), which analyzes the grayscale to extract the bone's cellular structure and density.

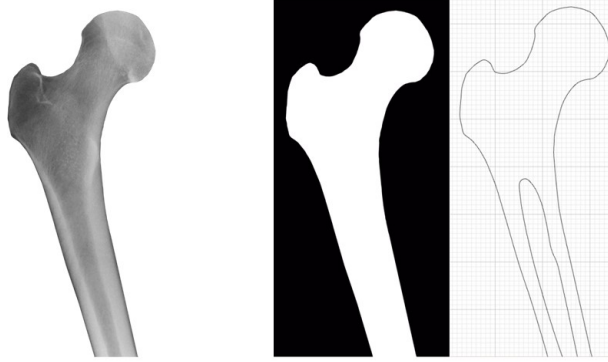


Fig. 17 Left: Radiography of the femoral head used for the example of the method. Center: Alpha layer of the radiography. Right: Outline obtained.

Fig. 17 (center) displays the alpha layer from the radiography, which defines the external bone geometry. Next, two clouds of points are generated according to the algorithm in section (1.2.1.2): a random cloud (Fig. 18- left) and another organized in a triangular grid (Fig. 18 - right). For each approach, three different density clouds of points are proposed, with decreasing densities (Fig. 18). The final clouds of points are obtained after eliminating points according to  $\rho_i$  and combining them, as seen in Fig. 18 (bottom-left for random and bottom-right for organized).

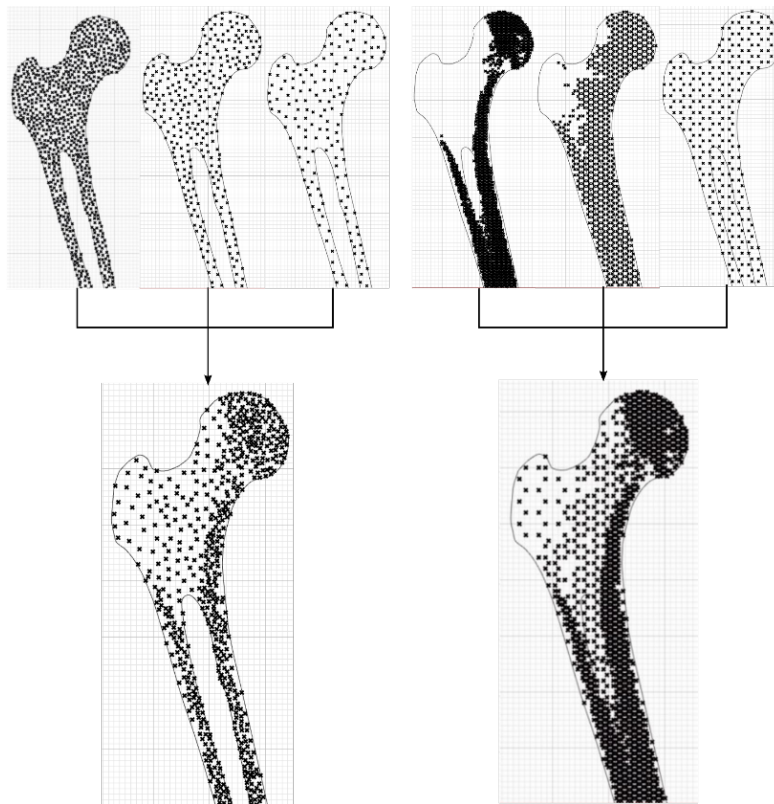


Fig. 18 Results obtained from the random point cloud (left) and the organized point cloud (right).



The two point clouds were used to develop Voronoi and Delaunay structures, as well as triangular organized structures. These structures were delimited by the contour of the analyzed geometry to create final cellular structures Fig. 19, which were saved as STL files and manufactured using a three-dimensional Object Eden 260 printing system (Stratasys, Eden Prairie, Minnesota, USA). The printed structures were embedded in support material that was later removed and were manufactured at a high resolution of X-axis: 600 dpi; Y-axis: 600 dpi; Z-axis: 1600 dpi. (Fig. 20).

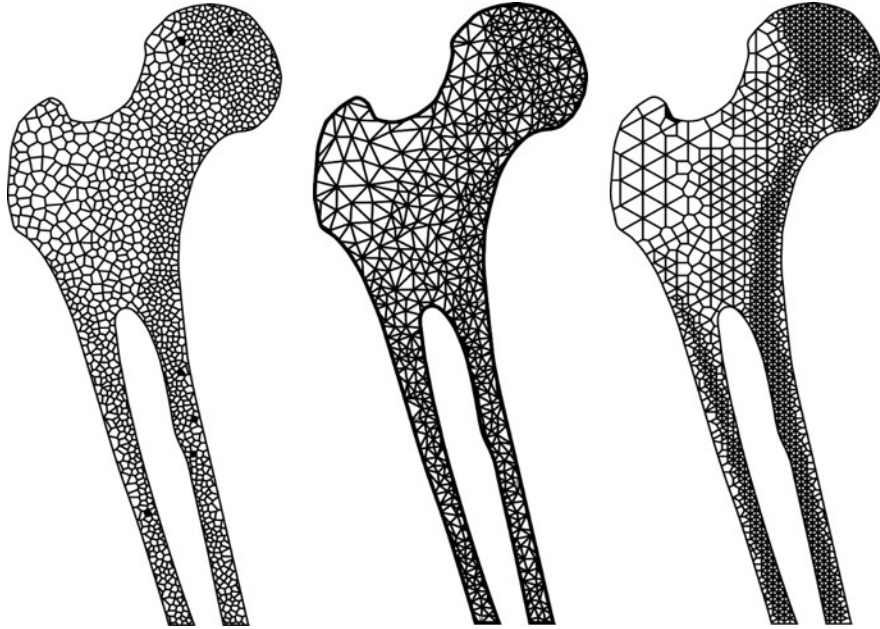
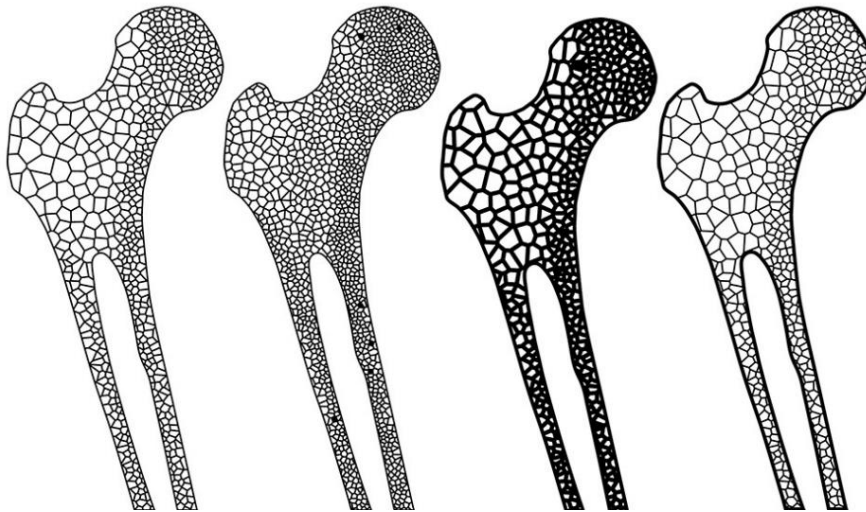


Fig. 19 CAD models obtained from the application of the method by regular algorithms. From left to right: regular Voronoi, regular Delaunay and regular triangular mesh.



*Fig. 20 Additive manufacturing results of CAD models derived from radiography.*

Furthermore, as shown in Fig. 21, the method allows control over the thickness of the trabeculae, the thickness of the external wall of the structure, and the number of pores to be handled.



*Fig. 21 Results on the possibility of iteration of the method: Voronoi with 581 pores, Voronoi with 1266 pores, increasing the thickness of internal trabeculae and increasing the thickness of the external wall.*

For further analysis of the application of the proposed methodology, it is important to evaluate the porosities obtained, to which the definition of absolute porosity is applied (Eq. 1):

$$\emptyset = \frac{V_p}{V_t} \quad \text{Eq. 1}$$

where  $\emptyset$  is the absolute porosity of the scaffold,  $V_p$  equals the volume of empty spaces and  $V_t$  is the total volume (empty spaces plus the total mass of the solid). The results for different tests are shown in Fig. 22. Bones have a layer of cortical bone with a porosity ranging between 10-30% and a spongy interior with a porosity that varies between 30-90% [40], [41], which are equivalent to the porosity obtained with values between 49-70% of porosity.

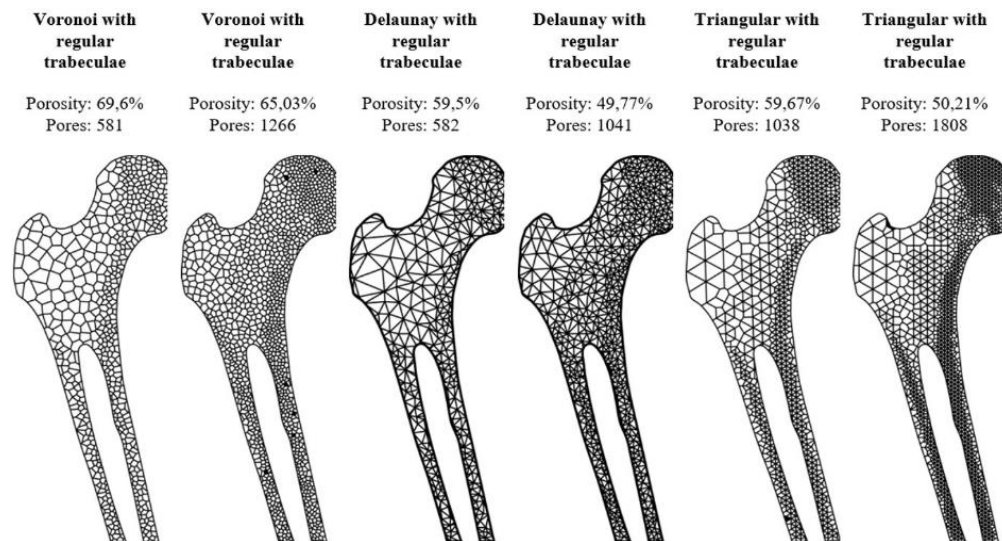


Fig. 22 Porosity values for the results obtained from the application of the algorithm of regular trabeculae as presented in [42].

### 1.2.2.2. Model validation by FEA

The proposed methodologies in sections 1.2 and 1.3 were validated using FEA simulation. A rectangular structural element subjected to compression was optimized using the power law approach [43], [44]. The optimized geometry had full density passive zones at the top and bottom and a fixed bottom boundary, except for the center node, which was allowed to move horizontally (Fig. 23). The optimization objective was to minimize compliance (deformation energy), and the optimization problem was solved using optimality criteria (OC), which is a heuristic updating scheme. A filtering process was used to ensure the existence of solutions in the design space, resulting in an optimal solution for minimal compliance and maximum stiffness.

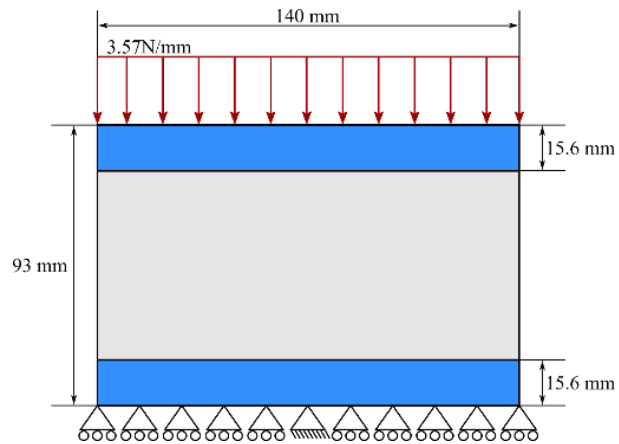


Fig. 23 Boundary conditions for the optimization algorithm as presented in [42].

The TO algorithm enables control of the desired volume fraction for material optimization. The study analyzed results for volume fractions of 40%, 60%, and 80% (Fig. 24). with material properties based on GREY FLGPGRO4 resin. The optimized geometries featured three columns (two lateral and a central) and a roof, with the central column and roof diminishing as the volume fraction decreased.

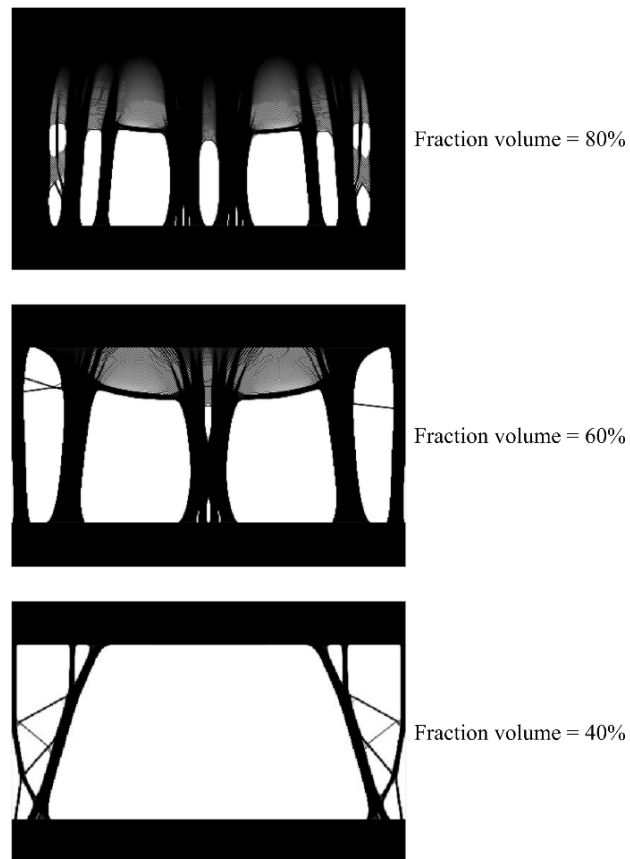


Fig. 24 Results obtained from the TO algorithm for different volume fractions: 40%, 60%, and 80%, as presented in [42].

Afterwards, following the methodology explained in section (1.2.1.2), 3 sets of random and organized point clouds were generated for each Fraction Volume model. The random clouds were used to create a Delaunay and Voronoi mesh, while the organized clouds were used to create a triangular equilateral mesh. Three meshes were evaluated for each Fraction Volume (Fig. 25).

Finite element analysis was performed on the tessellated geometries using a frame formulation with properties based on 3D CAD measurements of the cellular materials. The boundary conditions were the same as those used in the optimization algorithm (Fig. 23).

The displacement distribution was calculated for each of the fraction volumes (Fig. 25). with the Voronoi structure showing greater displacements at 40% and 60% Fraction Volume, while the triangular equilateral structure deformed the most at 80% (Fig. 25).

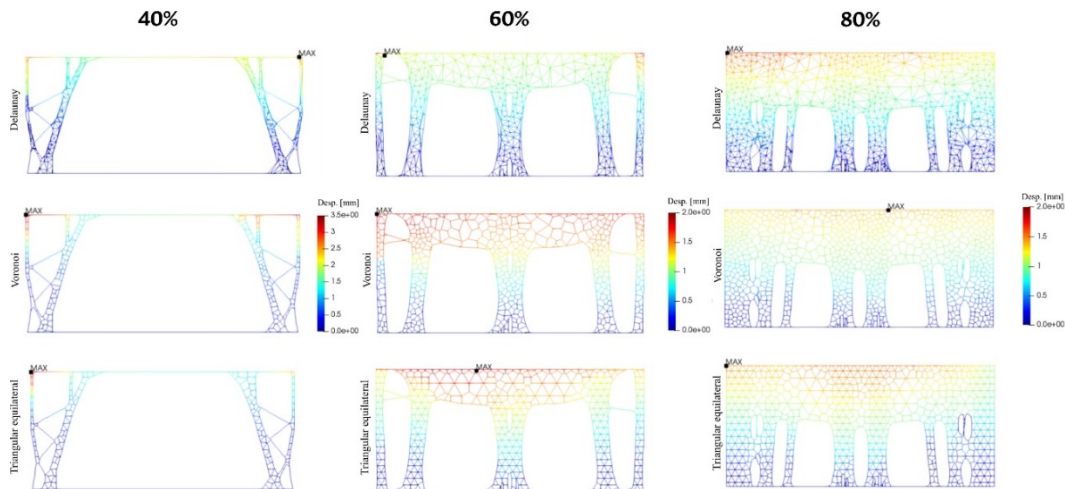


Fig. 25 Displacement fields in specimens using frame elements as presented in [42].

### 1.2.2.3. Experimental model validation

Further confirmation for the proposed method is carried out via compression tests on 10 cellular structures – random Voronoi (40%, 60%, 80%), random Delaunay (40%, 60%, 80%), equilateral triangles (40%, 60%, 80%), and a geometry without TO (100%, a square of material) – which were AM by using Formlabs-2 printing system (Formlabs, Somerville, Massachusetts, USA) (Fig. 25). This system uses stereolithography technology that operates by focusing an ultraviolet (UV) laser on a container of photopolymer resin. The structures were printed on Gray resin at a 0.1 mm layer thickness resolution.

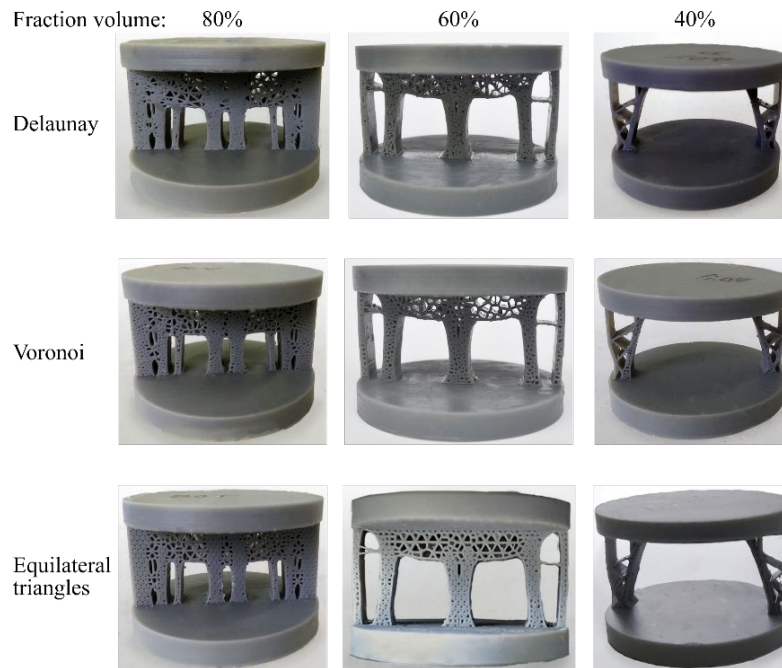


Fig. 26 3D-printed structures with Delaunay, Voronoi and equilateral triangles for fraction volumes of 80%, 60% and 40%, as presented in [42].

The 10 specimens were subjected to a compression test in which a compression load was applied with a velocity of 0.5 mm/min, and specimens were tested for failure by fracture. The testing apparatus used was a Shimadzu model AG-X plus of 300 kN (30 Ton), with the software Trapezium X. The load and crosshead displacement data were recorded using the A/Data hardware and software solution produced by the same manufacturer. The recorded force vs. displacement for all 10 specimens is shown in Fig. 27. It can be observed that the behavior of the different cellular structures was similar with a fraction volume of 40%. When the fraction volume increases (60%), the Voronoi structure is able to hold more loading. At the greatest fraction volume (80%), Delaunay and Voronoi structures had a similar behavior (Fig. 27).

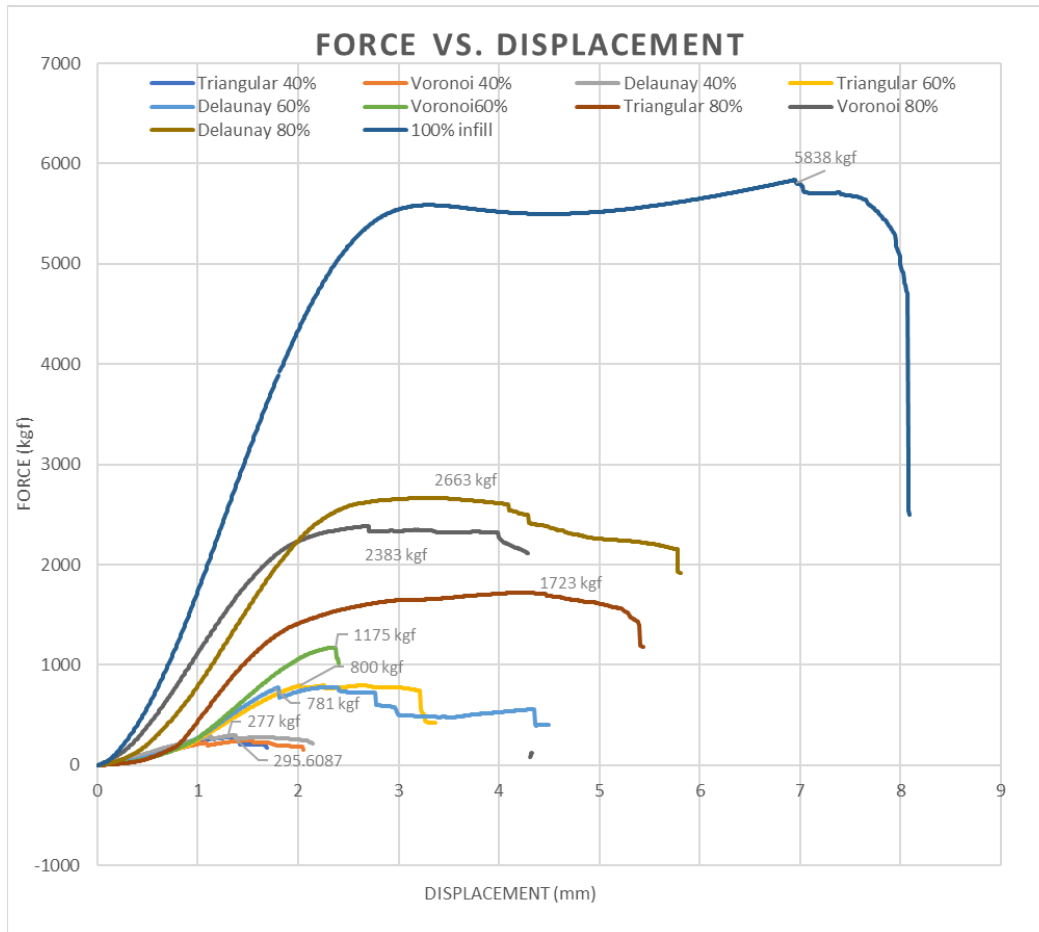


Fig. 27 Force (kgf) vs. displacement (mm) for all the tested specimens [42].

Moreover, the failure trajectories were also analyzed for each structure and percentage of fraction volume (Fig. 28, Fig. 29 and Fig. 30). For low percentages (40% and 60%), the first element to fail was one of the lateral columns; however, for high percentages (80%), the first failure occurred between one of the lateral columns and the one in the middle.

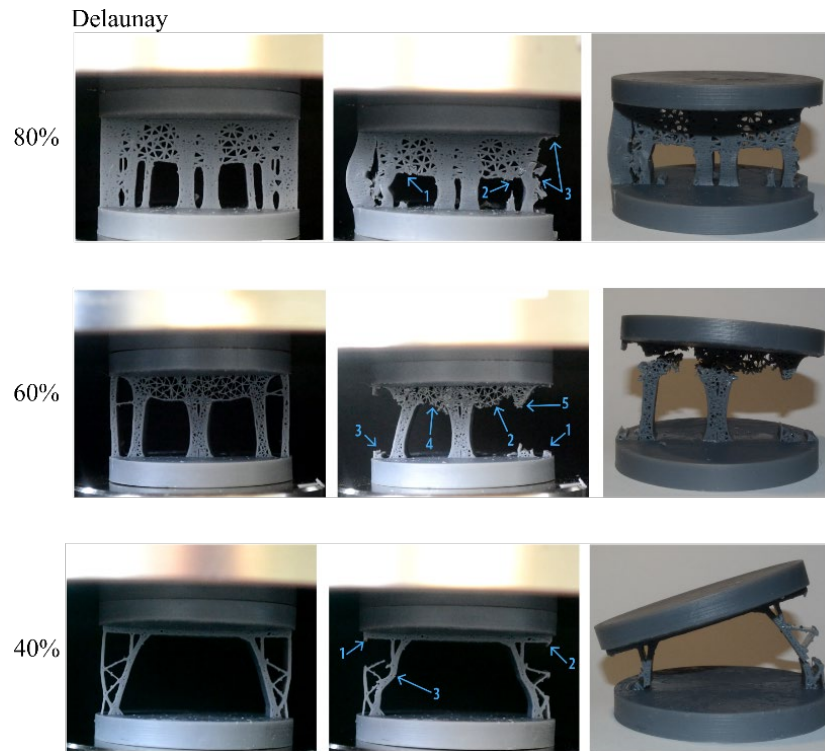


Fig. 28 Failure of the Delaunay cellular structures with fraction volumes: 80%, 60% and 40% [42].

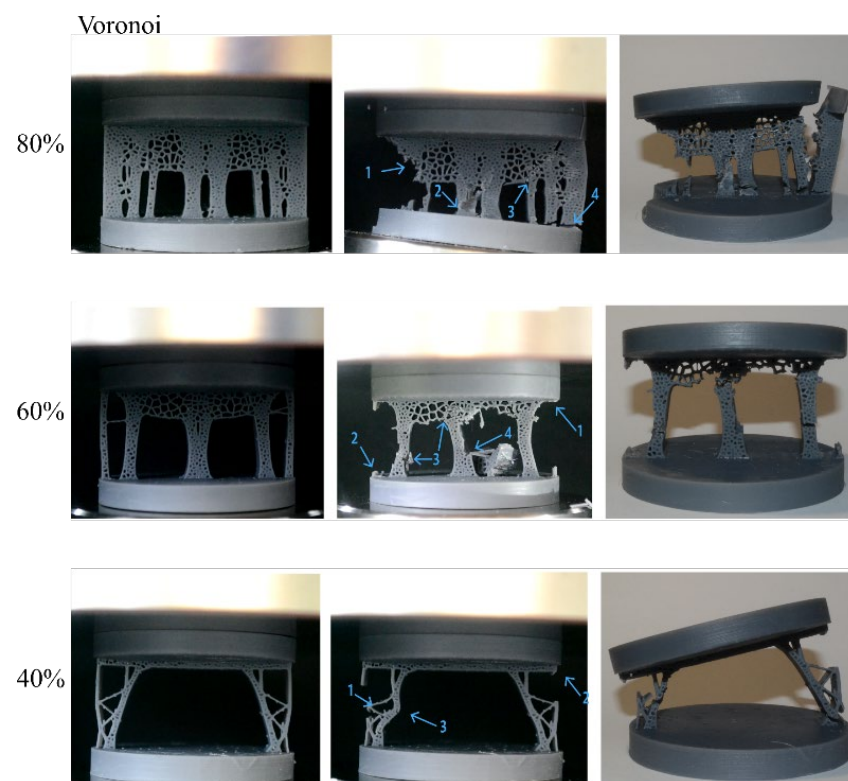


Fig. 29 Failure of the Voronoi cellular structures with fraction volumes: 80%, 60% and 40% [42].



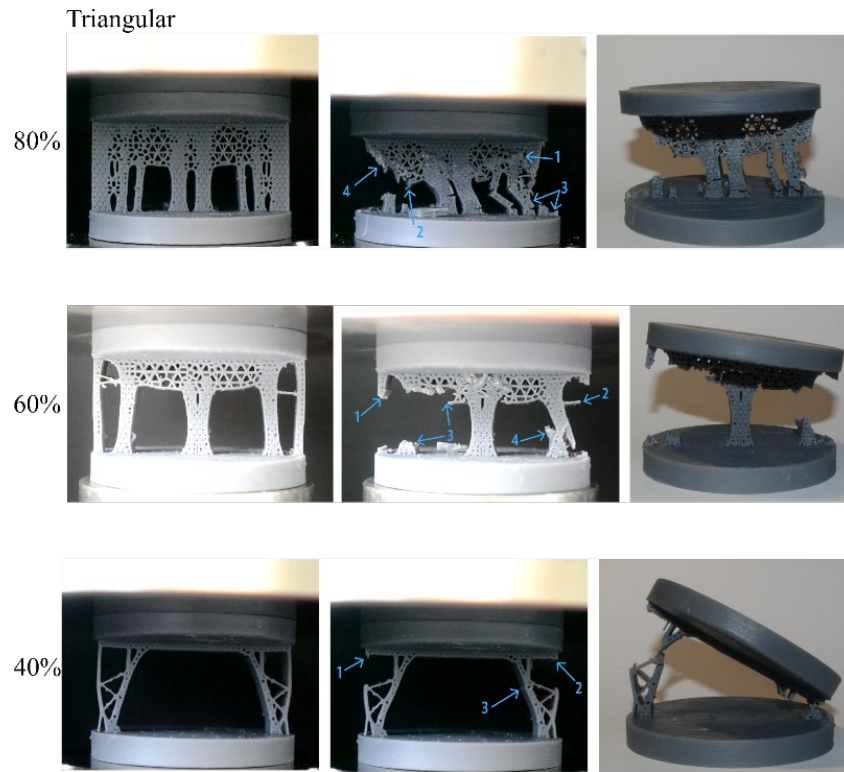


Fig. 30 Failure of the triangular cellular structures with fraction volumes: 80%, 60% and 40% [42].

## 2. Proposed algorithm for the design of scaffolds for bone tissue regeneration using diagnostic images.

The scaffold architecture will be determined and controlled using an algorithm that implements different image-based design parameters. Image-based design is an alternative method for designing and manufacturing scaffolds for specific patients and sites [23], [30]. This method blends available image processing and management techniques, computer-aided design software, and different manufacturing methods to accelerate the design process and subsequent fabrication of scaffold microarchitectures [23].

### 2.1. Parameters for the design of 3-D scaffolds

There are many parameters that can affect cell behavior in a controlled manner. The complex interaction of these parameters makes it necessary to have as much control as possible over the scaffold design. In this way, the influence of different physical, chemical, and biological properties on cell behavior can be tested [45], [46].

Some of the most important parameters to consider are:

- Pore size determines cell infiltration, migration, and proliferation. It also affects oxygen and nutrient exchange [47]–[49].
- Porosity affects cellular accommodation and adhesion, as well as bone vascularization [47], [50]–[53].
- Pore interconnectivity: Determines the final geometry and its vascularization [49], [54]–[56].
- Mechanical properties: Ideal for obtaining an equivalence in stress distribution and retaining a three-dimensional structure that allows tissue growth [57]–[60].
- Degradation: This process allows deposition of the extracellular matrix by the growing tissue and provides structural support until the native matrix is deposited [51], [54], [61]–[64].
- Biochemical signaling: Provides stimulation for vascularization, adhesion, proliferation, and cell differentiation [60], [65]–[67].

Since the algorithm focuses mainly on the physical geometry of the scaffold, three initial parameters of those mentioned above will be used: pore size, porosity, and pore interconnectivity. On the other hand, the mechanical behavior will be evaluated to obtain feedback. Additionally, as an image-based design method, the definition will also be fed from diagnostic images obtained by computed tomography.

These parameters are interrelated, allowing the control of the geometry through different methods, such as the location of the porogenic points, initial concentration of points, pore size, scaffold shape, trabecula thickness, and percentage of porosity. At the same time, to have greater control over the generation of a specific internal microarchitecture for the patient, the information obtained from the processing of diagnostic images will be used as a basis for obtaining the final result [30].

## 2.2. Code generation

A generative and parametric design algorithm is proposed, which, from diagnostic images representing a field of densities, determines the formation of the internal structures using Voronoi diagrams. The tool was implemented in the Grasshopper program (McNeel, USA). Grasshopper is an algorithm editor integrated into the modeling software Rhinoceros 3D Ver. 7 (McNeel, USA).

### 2.2.1. Adapting the algorithm with Voronoi to 3D

The algorithms proposed in section 1 were adapted for handling computed tomography images, and with this, it is possible to generate a solid in 3 dimensions. Likewise, the algorithm and the development of the CAD model are designed in Rhinoceros 7.

**Step 1.** The algorithm processes each bone scan and divides them into their AHSL channels, which correspond in their order to Alpha channel, Hue, Saturation, and Luminance. Using the luminance channel, the image density  $\rho$  values are determined, which are then assigned to each image pixel.

**Step 2.** The algorithm detects each bone scan's internal and external contours using the alpha channel and generates the corresponding curves for each diagnostic image (Fig. 31).



Fig. 31 The white curves form the general external geometry of the bone.

Subsequently, each curve is placed on the Z-axis at the correct distance using the information obtained from the diagnostic images. In this case, each image was located 0.6 mm from the other (Fig. 32). Additionally, the contours are used as topographic lines to generate a solid surface (Fig. 33).

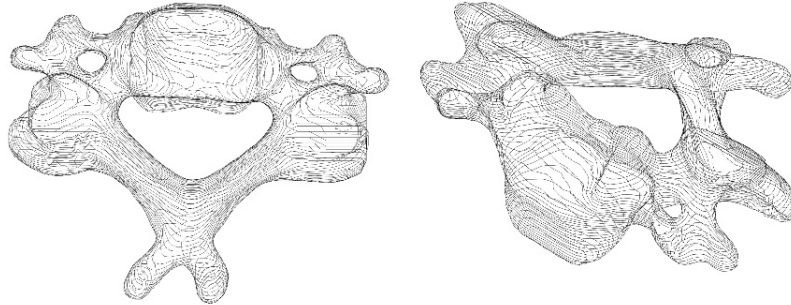


Fig. 32 The contours are located on the z-axis forming the topographic lines that describe the external architecture of the bone.

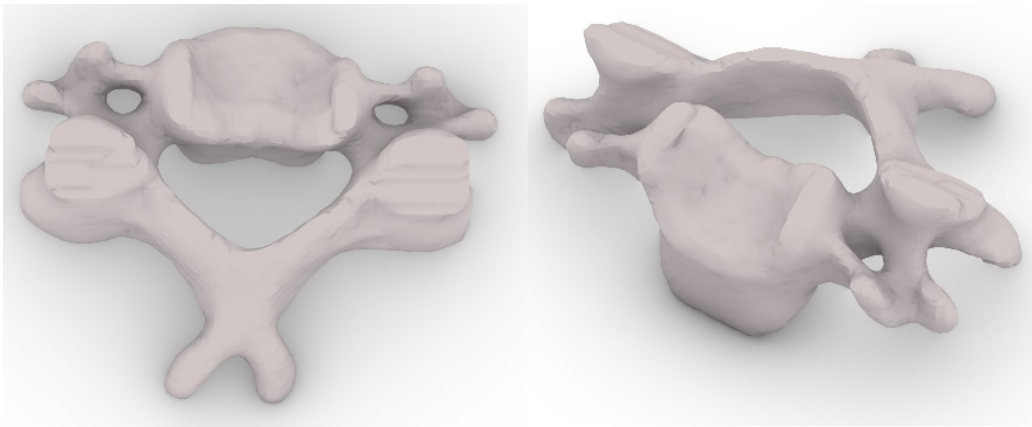
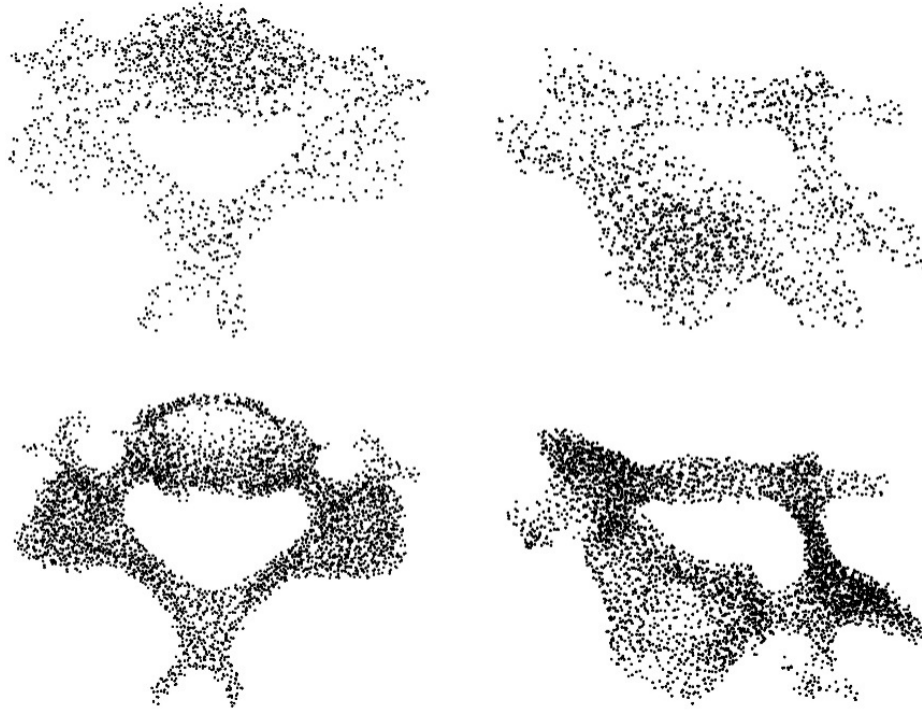


Fig. 33 Solid surface created from the topographic lines.

Once the outer limits are set, two point clouds are generated and distributed within the contour. The first point cloud will have a number of points =  $a$ , designated by the user, while the second point cloud will have a number of points =  $b$ , which always satisfies the condition of  $b < a$ . The points are then distributed using the density  $p_i$ , which is directly related to the gray values of the image, with the absolute black value density  $p_i = 1$  and absolute white density  $p_i = 0$ . Because of this, the areas of the image where the density  $p_i$  is close to 1 will obtain a higher point density, and the areas where  $p_i$  is close to 0 will obtain a lower point density (Fig. 34).



*Fig. 34 The two point clouds generated within the contours of the bone are shown.*

**Step 3.** The pi density values are separated into two distinct domains, which are assigned for each point cloud generated in the previous step. Once the values are assigned, both clouds are merged into a single group containing all the points along with the pi values corresponding to the bone domain. The final point cloud generates a 3-D Voronoi diagram where the solid surface will be divided into closed polyhedra, with the condition that each one coincides with the face of the adjacent polyhedron (Fig. 35).

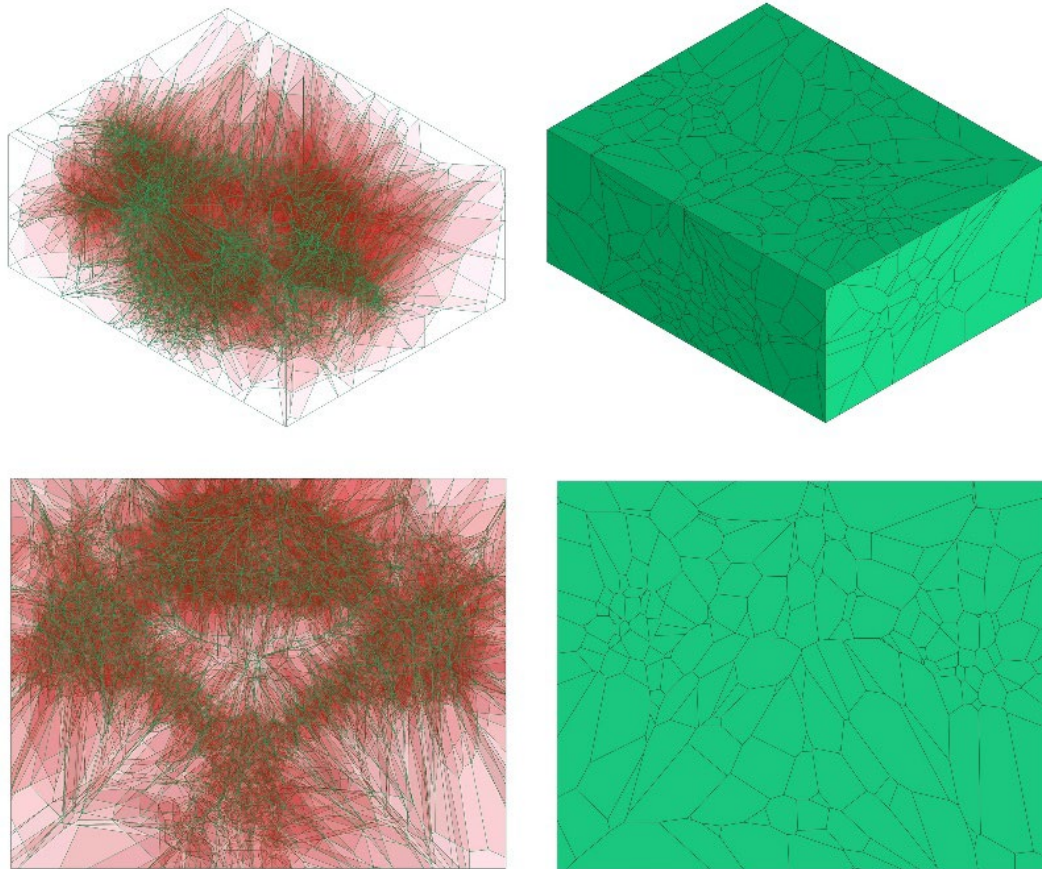
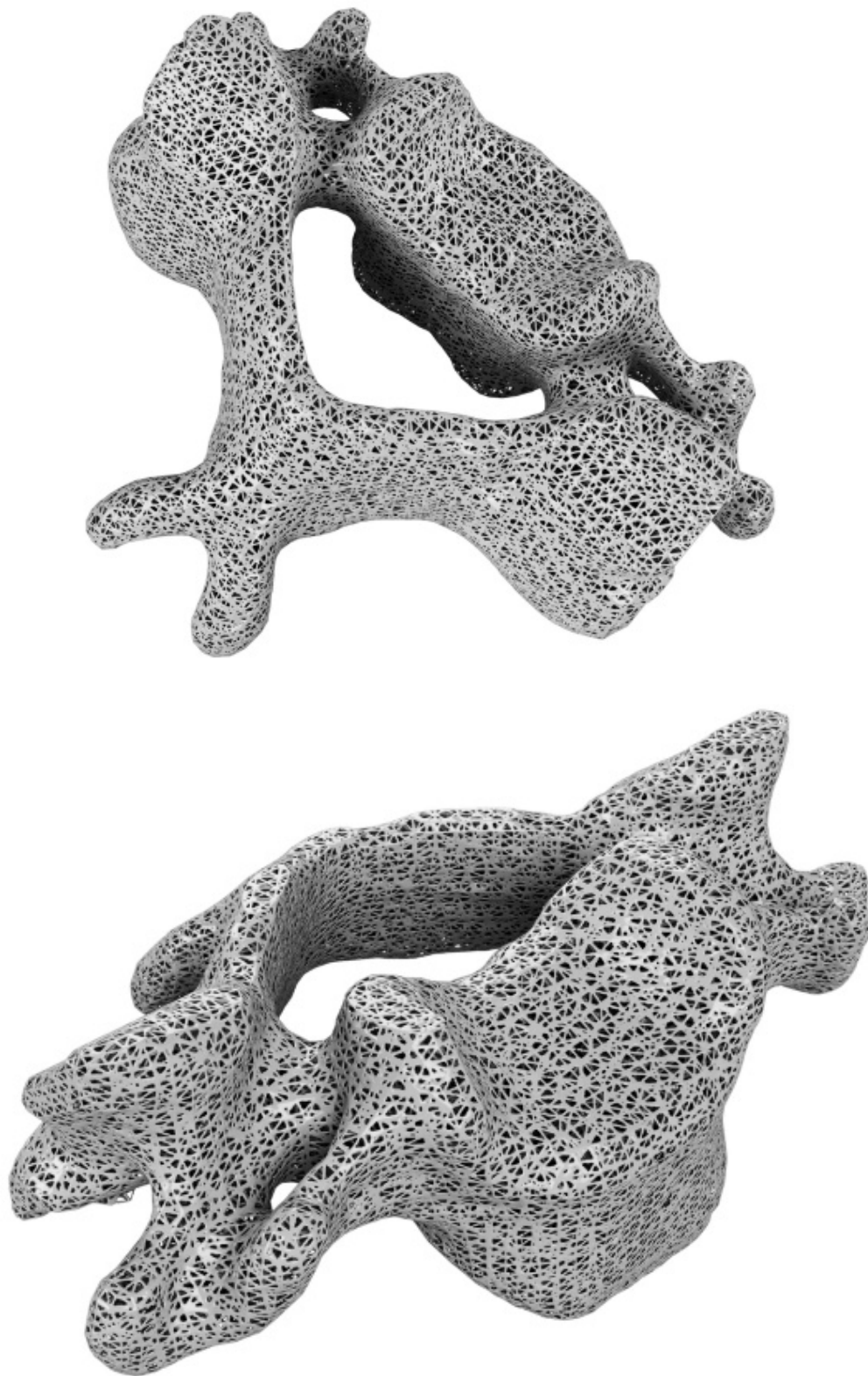
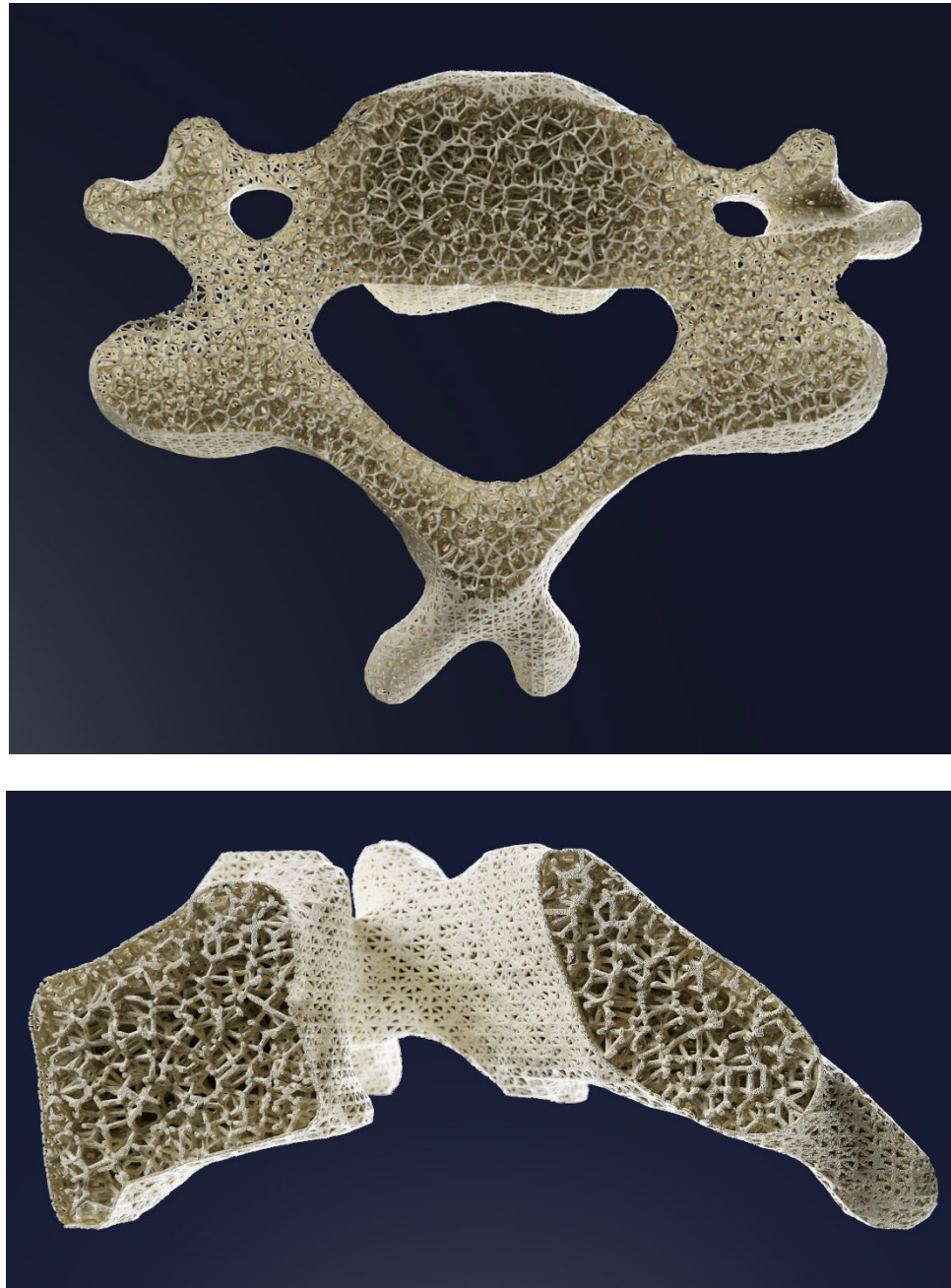


Fig. 35 The generated Voronoi diagram is placed inside a bounding box with the minimum dimensions corresponding to those of the bone.

**Step 4.** Using the solid surface resulting from step 2 (Fig. 33), a Boolean operation is performed to eliminate the parts outside the solid surface that do not correspond to the bone (Fig. 36). Likewise, other different geometries can be used to segment parts of the bone. Finally, using the edges of the polyhedra and a designated width, the corresponding trabeculae are generated inside the solid, resulting in a porous material (Fig. 37).



*Fig. 36 Outer surface of the bone, generated after the Boolean operation.*



*Fig. 37 Axial and sagittal cross-sections demonstrating the internal architecture of the bone generated using the established trabeculae width.*

The result is a porous structure whose internal architecture is built by trabeculae forming a network of interconnected pores, ready to be fabricated by additive manufacturing (Fig. 38). In addition, the relative density of the material is controlled from the diagnostic images, and it is directly related to the density information obtained from them (Fig. 39). In this way, the different density and porosity ratios found in the bone are preserved (Fig. 40).



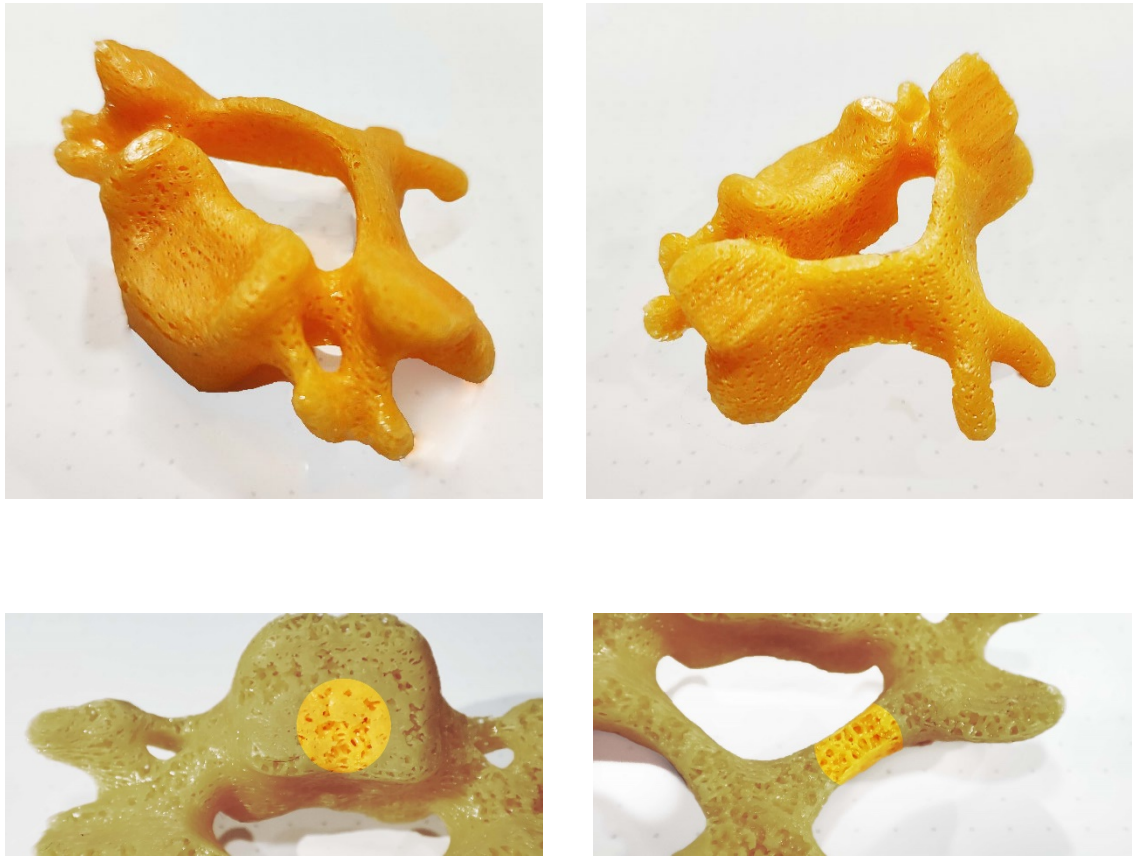


Fig. 38 Additive manufacturing result of the CAD model derived from the diagnostic images.

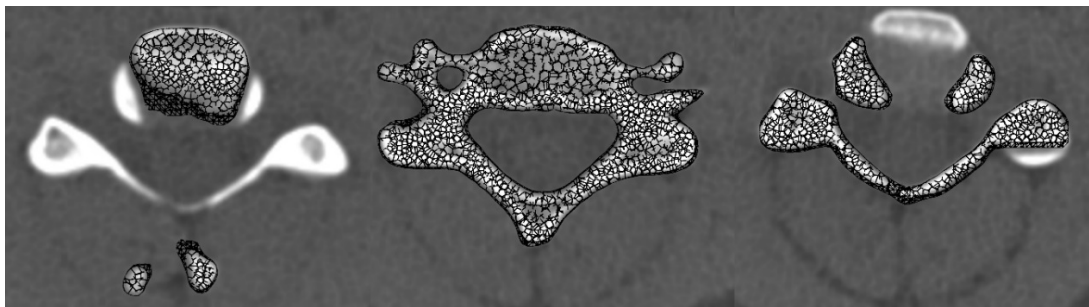


Fig. 39 Three slices at different heights of the Z-axis of the generated structure and their relation to CT scans at the same height in the bone are presented.

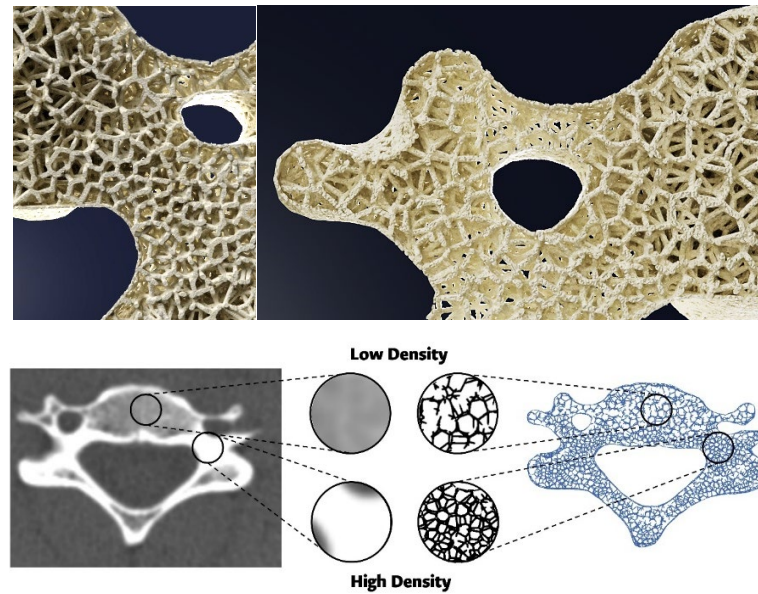


Fig. 40 The relation of the low and high material density zones concerning their counterparts in the generated porous structure.

The proposed algorithm is shown in Fig. 41. With this algorithm, a porous solid is generated from CT scans, in which the number of pores will be controlled, as well as the size of the trabeculae, and they are directly related to the information obtained from the initial diagnostic images.

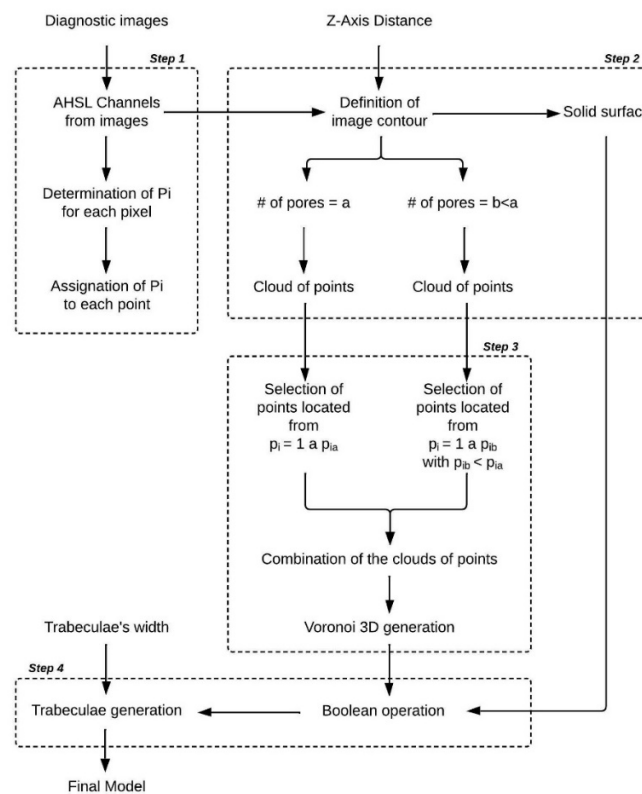


Fig. 41 Algorithm for the generation of a porous solid from diagnostic images.

The resulting algorithm was finally implemented in Grasshopper, which is a tool within Rhinoceros 7 that allows the different geometry variables of the scaffold to be easily and quickly altered. In addition, it has tools for the development of generative design through the use of Galapagos, an internal tool of the software, for the use of genetic algorithms to generate multiple responses for the same structure.

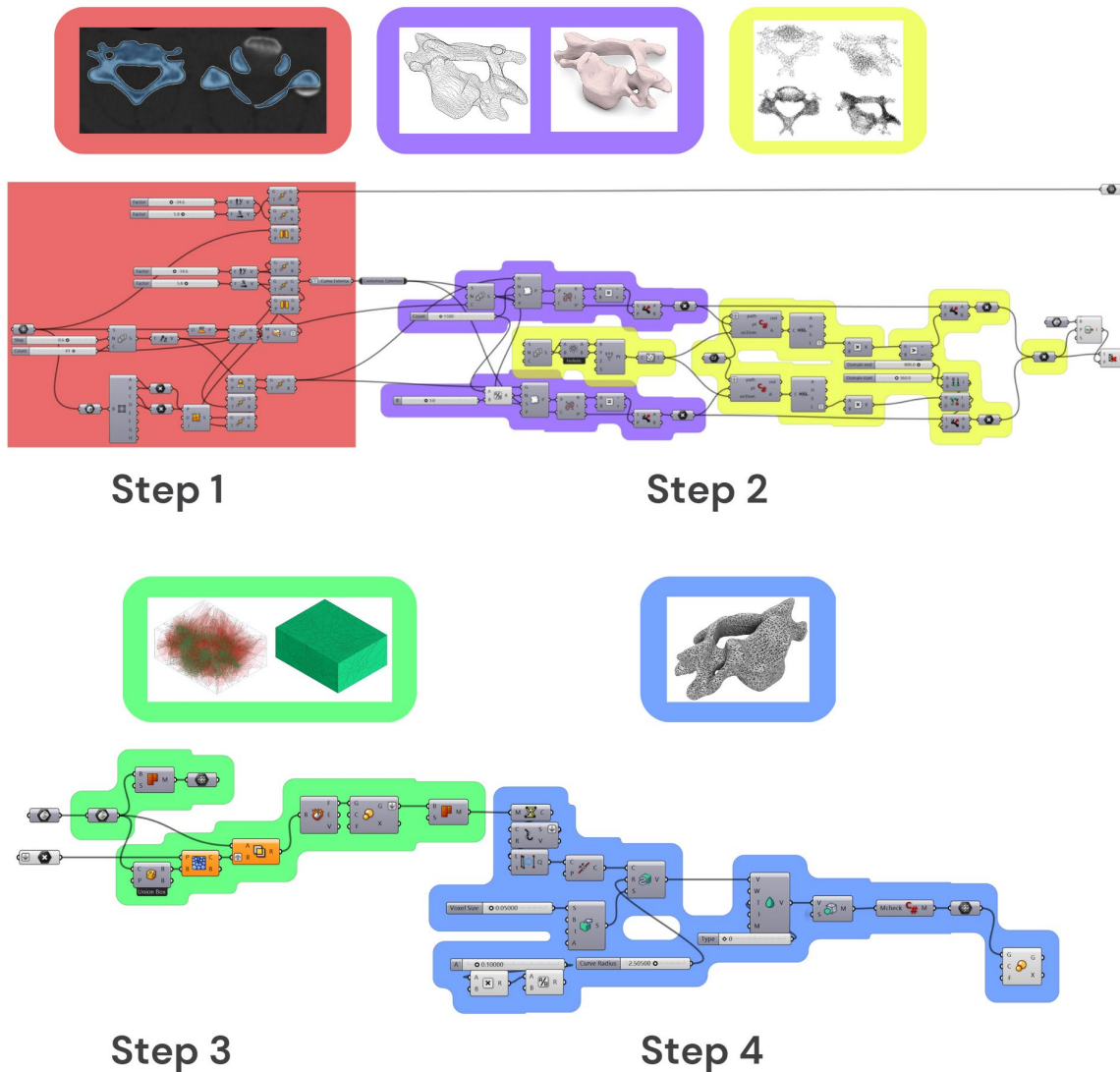


Fig. 42 Algorithm for the generation of a porous solid from diagnostic images as implemented in Grasshopper.

### 3. Application of the algorithm in the interpretation of bone

The proposed algorithm was used on a series of human neck and skull CT scans, focusing on the C7 vertebra. For comparison of the results, a 5 mm x 5 mm x 5 mm pig bone specimen was also scanned. Additionally, to maintain the same dimensions of the pig specimen and to be able to compare results, the geometry obtained by the algorithm was segmented into a 5 mm cube within the body of the human vertebra and subjected to finite element analysis, determining its apparent Young's modulus. Subsequently, 4 types of specimens were fabricated using additive manufacturing, and these specimens were later used in a compression test to review the results and characterize the mechanical behavior.

#### 3.1. FEA Simulations

A schematic of the process to generate a porous solid is illustrated in Fig. 41. Rhinoceros software and its Grasshopper module are used to design the scaffold architecture and calculate its different porosities to generate different combinations of parameters to obtain different specimens. Finite element analysis (FEA) simulates the mechanical performance of each specimen to aid in the final selection and characterization of the scaffold. The different architectures were selected to observe the influence of the trabeculae width on the porosity of the solid and with the apparent Young's modulus. In conjunction with this, the results are compared with a control specimen from a pig bone scaffold (Fig. 43).

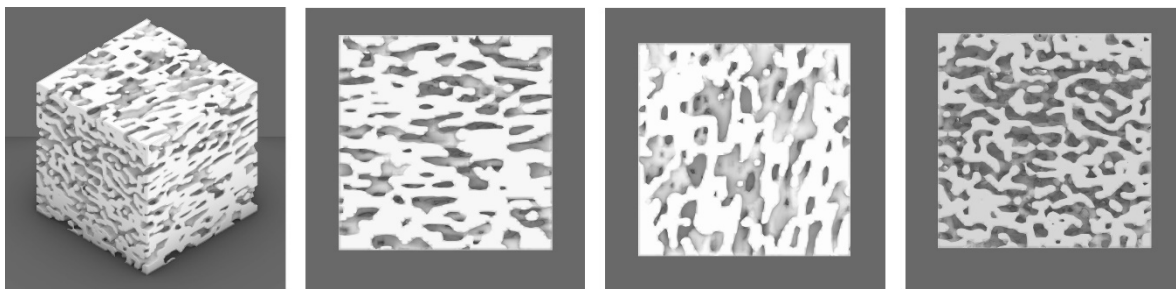


Fig. 43 Pig bone scaffold, with its main faces in the X, Y, and Z axes.

The scaffold geometry was defined based on literature parameters and adjusted according to the information obtained from the diagnostic images. For the solid domain, a 5 mm cube was placed according to the area of the vertebra with the highest compressive mechanical loads, approximately 500 N in axial compression, which is the average value of loading force taken for a person of 70 kg [68], [69]. Between the posterior medial and posterior external parts of the vertebral body (Fig. 44).

To design the structures, we started from the previously observed porous solid (Fig. 36), drew a 5 mm cube that corresponds directly to the dimensions of the pork bone scaffold, and then segmented the solid. The thickness of the trabeculae was varied to characterize its influence on the final mechanical behavior of the structure. Each of the scaffolds obtained was generated through CAD software (Table

1) to (1) calculate its porosity, correlating the solid and empty volume, and (2) obtain the 3D models required for the following mechanical simulations.

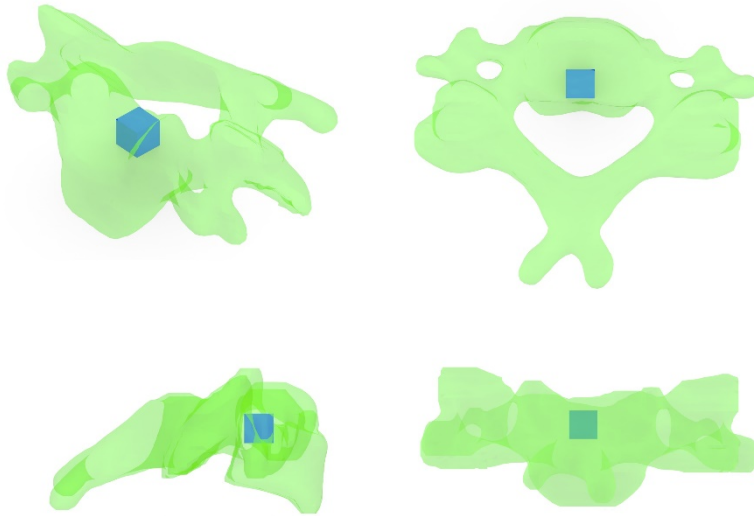


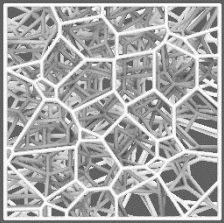
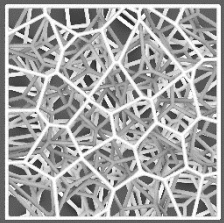
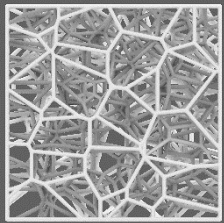
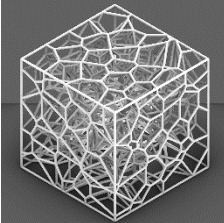
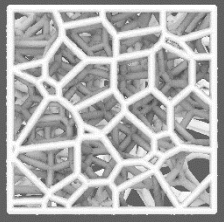
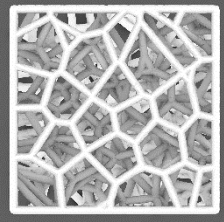
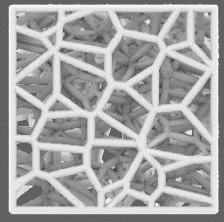
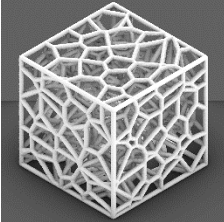
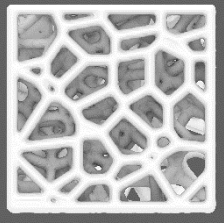
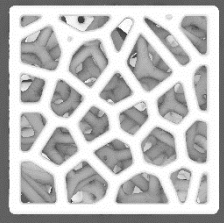
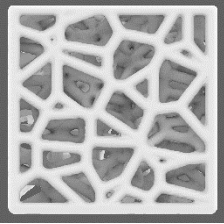
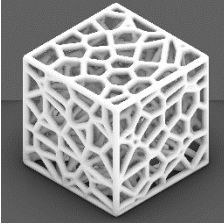
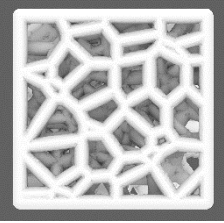
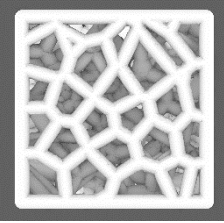
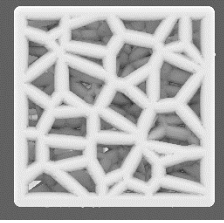
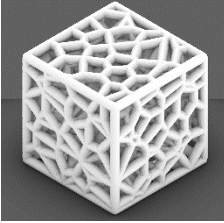
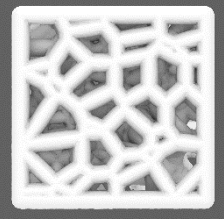
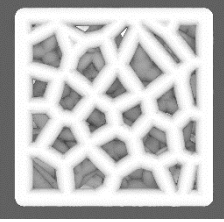
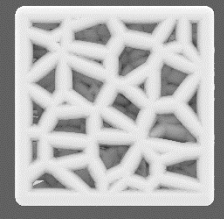
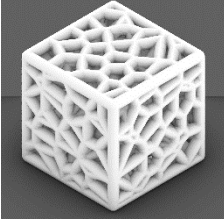
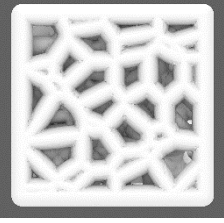
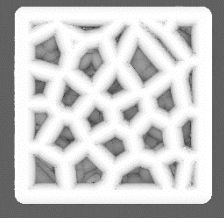
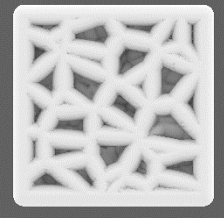
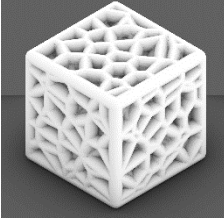
Fig. 44 The blue cube is the 5 mm cube within the body of the human vertebra to be used for the finite element analysis.

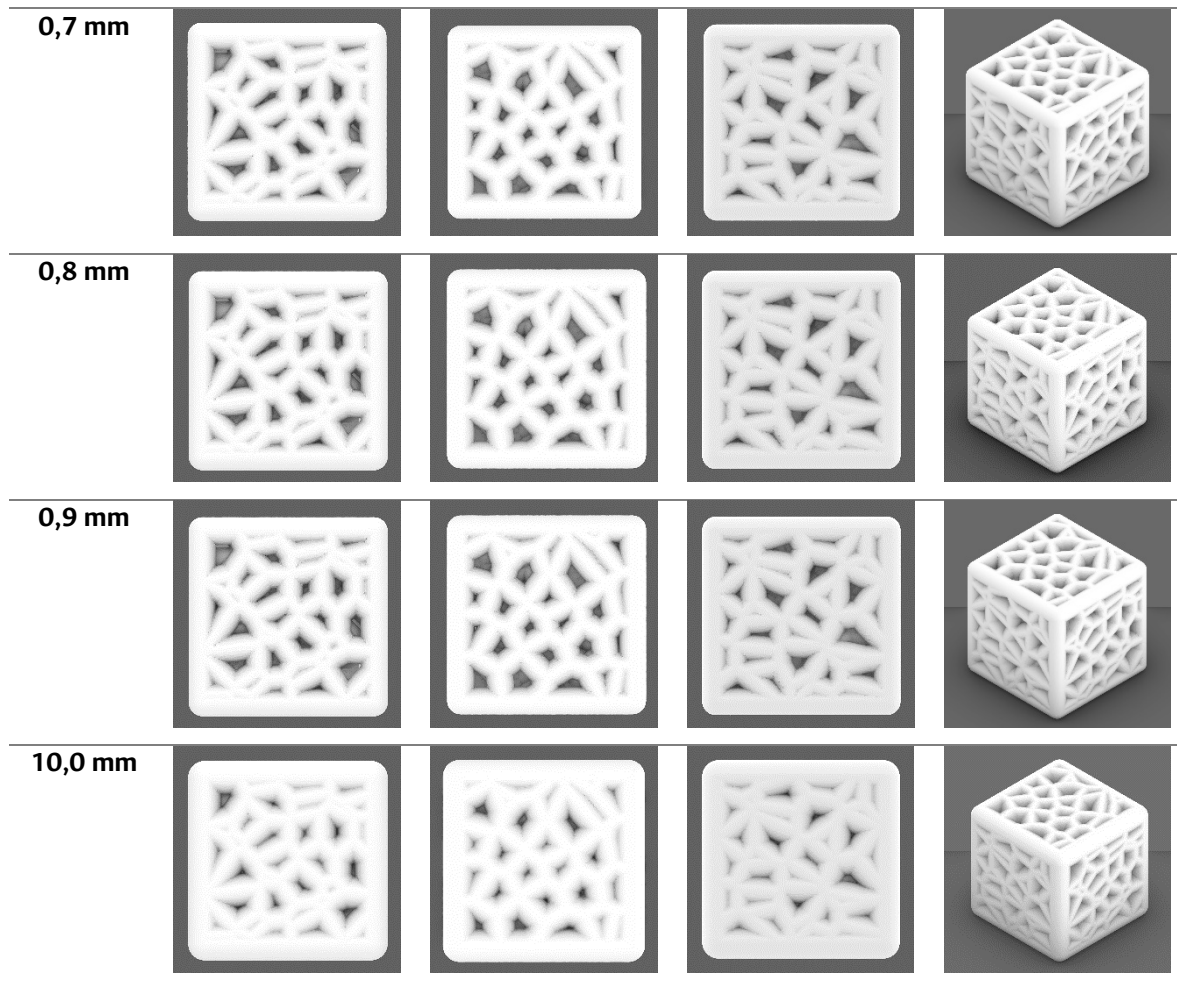
The absolute porosity of the scaffold will be defined as (Eq. 2):

$$\emptyset = \frac{V_p}{V_t} \quad \text{Eq. 2}$$

where  $\emptyset$  is the absolute porosity value,  $V_p$  is equal to the volume of void space, and  $V_t$  is the total volume (void space plus total mass of the solid). The results for the different structures are shown in Table 3.

Table 1 Scaffolds with a variety of trabecular widths

Trabecula width	Main Face X-Axis	Main Face Y-Axis	Main Face Z-Axis	Isometric view
0,1 mm				
0,2 mm				
0,3 mm				
0,4 mm				
0,5 mm				
0,6 mm				



Additionally, the algorithm allows information on the nominal pore size to be obtained to verify that it is within the necessary parameters that favor osteogenic differentiation, tissue integration, vascularization, and diffusion of nutrients and oxygen [70]-[74]. These values have been widely discussed in the literature and are between 30 and 600  $\mu\text{m}$  with interconnected pores [73], [75], [76].

Fig. 46 displays histograms generated by the algorithm, showing the distribution of pore sizes. Each nominal size is obtained by making the largest sphere that each cell can contain from its center and touching all the faces of the polyhedra, after which the diameter of the sphere is measured Fig. 45. The accompanying Table 2 lists the size range for each trabecular thickness and the number of pores in each structure. As the trabecular size increases, some pores disappear.

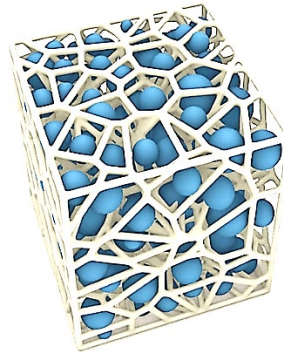
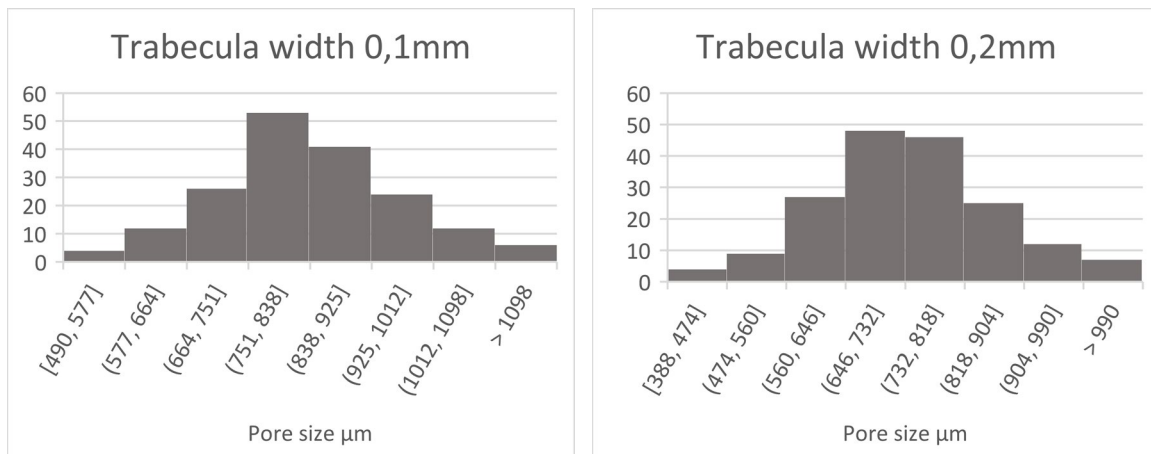


Fig. 45 Each cell in the cellular structure contains a sphere to measure the nominal pore size.

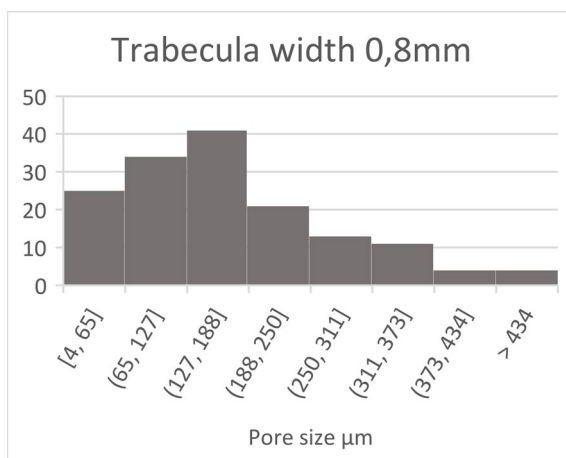
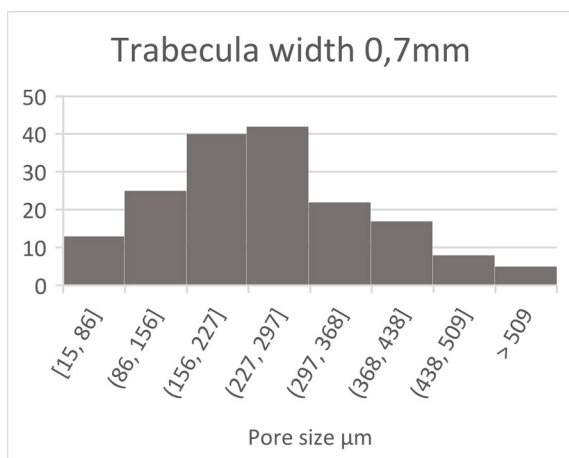
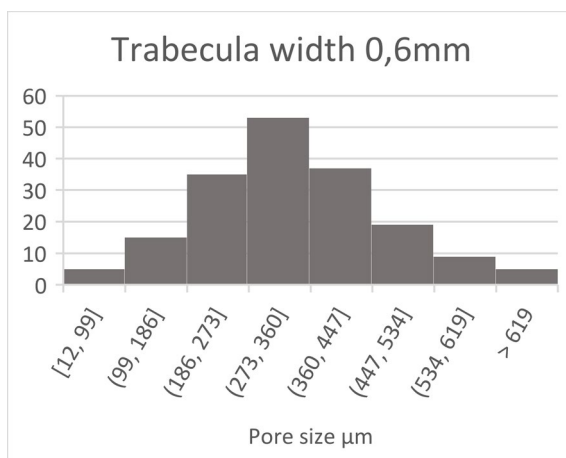
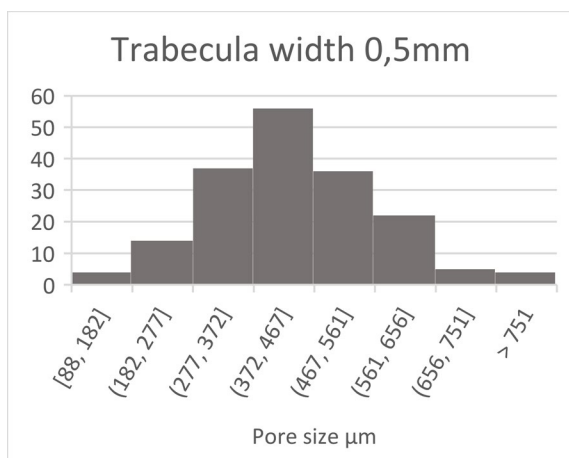
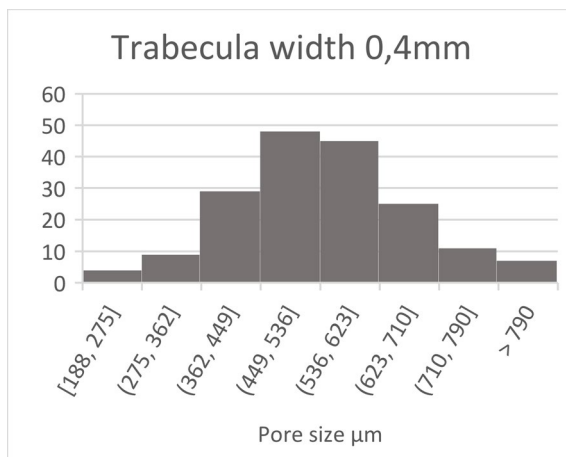
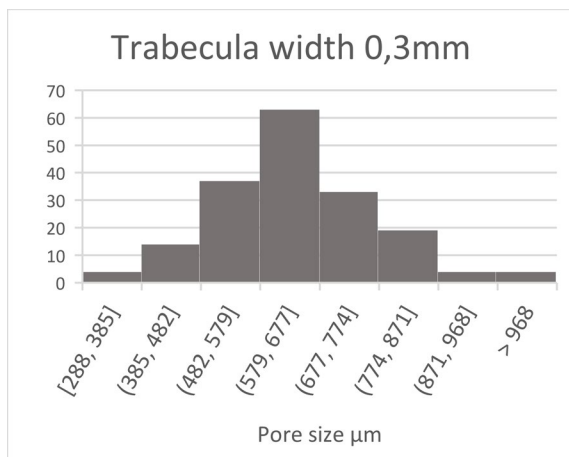
Table 2 Number of pores in each structure and size range

Trabecula width	Quantity of pores	Minimum size $\mu\text{m}$	Maximum size $\mu\text{m}$
0,1 mm	178	490	1395
0,2 mm	178	388	1295
0,3 mm	178	288	1195
0,4 mm	178	188	1095
0,5 mm	178	88	994
0,6 mm	178	12	895
0,7 mm	172	15	795
0,8 mm	153	4	694
0,9 mm	109	1	595
10,0 mm	51	0,3	493

#### PORE SIZE DISTRIBUTION HISTOGRAM







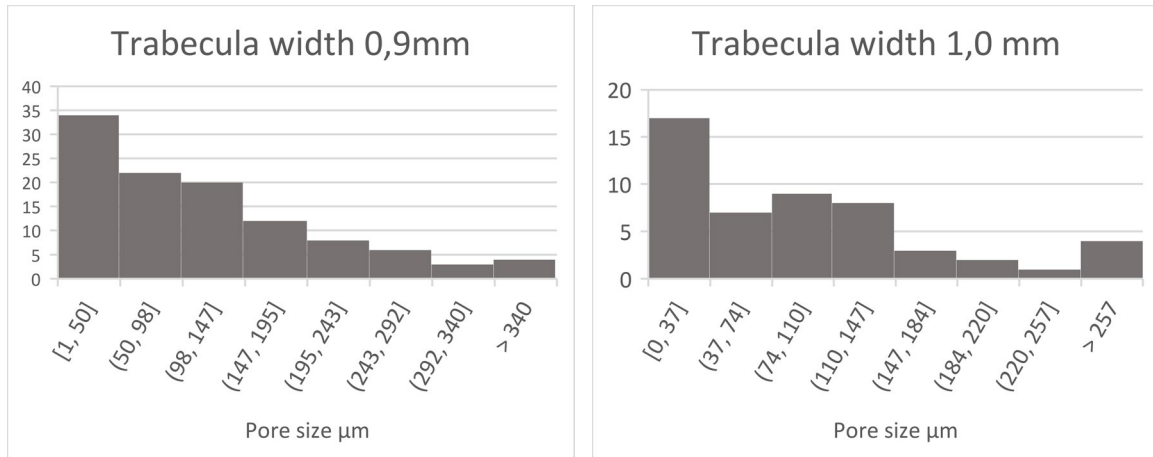


Fig. 46 Histograms showing the distribution of pore sizes for the different structures generated.

Finally, CAD models were prepared for mechanical simulation. To characterize the mechanical behavior, the apparent Young's modulus of each structure was found by axial compression (Fig. 47). For this test, three different displacement loading modes were performed, each one for the main axis of the cube (XYZ). The material used for the simulations has the properties of the photocurable resin that will be used in the subsequent manufacture of the different specimens (Table 3). For this, a characterization of the material was carried out using a solid cube manufactured via SLA (Fig. 47).

Table 3 Material properties obtained after characterization of the cube.

Material	Volume (cm <sup>3</sup> )	Density (g/cm <sup>3</sup> )	Mass (g)	Porosity	Force (N)	Young Modulus (MPa)
Photocurable UV resin	0.1312	1,25	0,164	0%	927,137	589,91

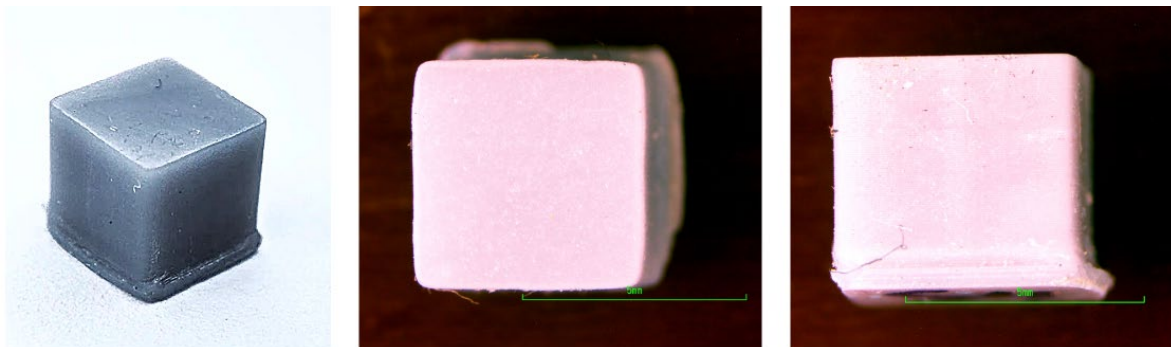


Fig. 47 Solid cube manufactured using SLA, the top face and one of the lateral faces can be appreciated, and the images were obtained using a stereomicroscope.

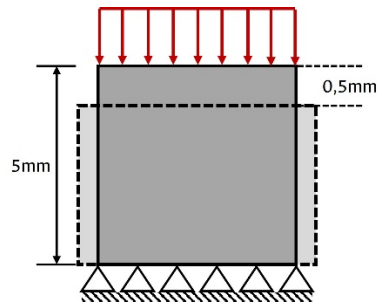


Fig. 48 side view showing the boundary conditions for the compression test.

This compression test is part of a method (Fig. 48) that consists of 6 steps to find and check Young's modulus: (1) a displacement of 0.5 mm is applied to the structure, (2) Young's modulus is found from the maximum stress and strain results, (3) the reaction force found on the fully restrained face of the structure is obtained, (4) Young's modulus found in step 2 is assigned to a solid cube, and a load equivalent to the reaction force from the previous step is applied, (5) the displacement result is calculated and compared with the displacement applied in step 1, and (6) the apparent Young's modulus is obtained.

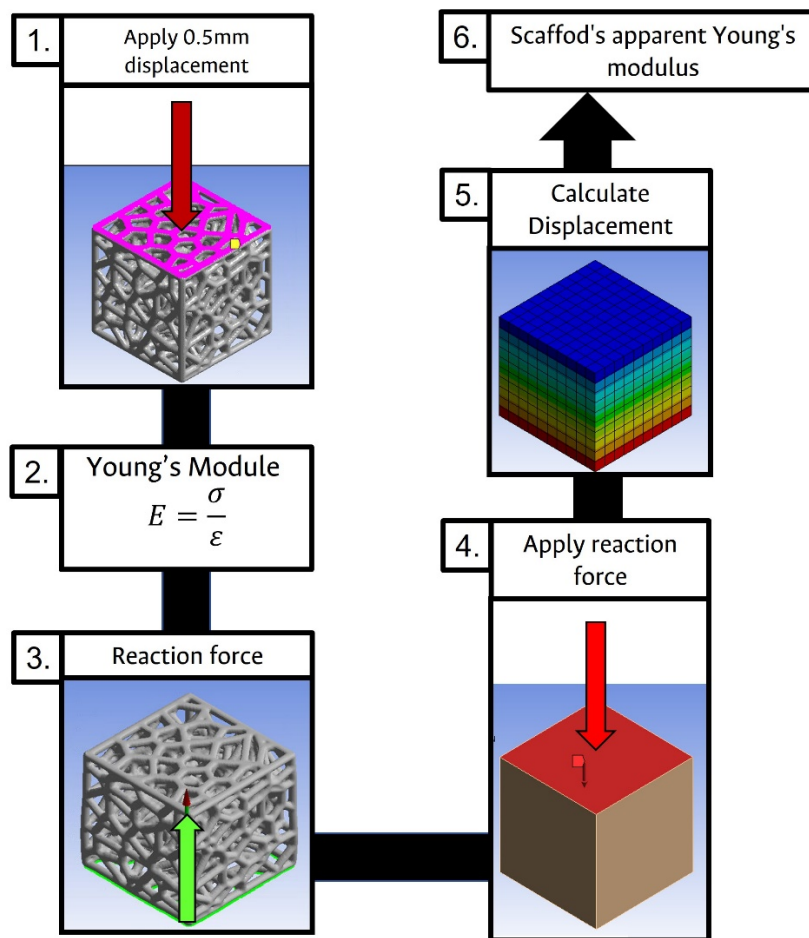


Fig. 49 Methodology to obtain the apparent Young's modulus of a porous solid.

This methodology was applied for each structure to corroborate the apparent Young's modulus; in addition, the modulus for each of the principal axes (XYZ) was found to verify the anisotropy of the geometry.

Finally, before applying the proposed method, a mesh convergence study was developed to determine the number of elements required in the model to ensure that the analysis results were not affected by the mesh size. For this analysis, an allowable change of 5% between the solutions was set as an input in Ansys Workbench 2022 R1 (Fig. 50).

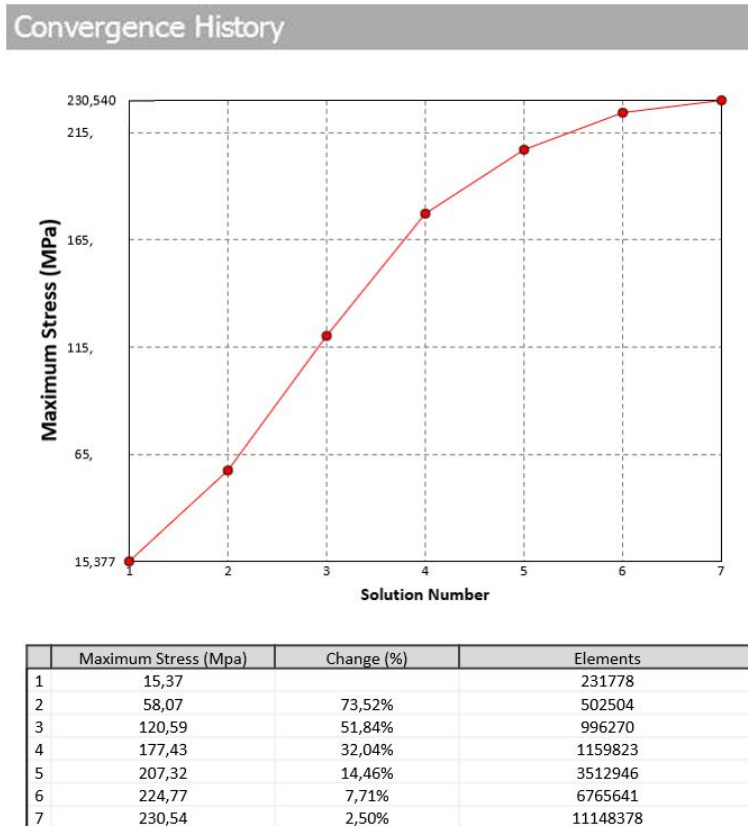


Fig. 50 Tabulated data showing iterations, stress value, % change and elements as presented in the worksheet by the software.

## 3.2. Results

### 3.2.1. Apparent Young's Modulus

Applying the methodology presented in section 3.1.1, the porosity percentage and apparent Young's modulus for the XYZ axes of the pig bone scaffold were obtained in Table 3. The figure shows the geometric model of the pig scaffold already imported into Ansys.

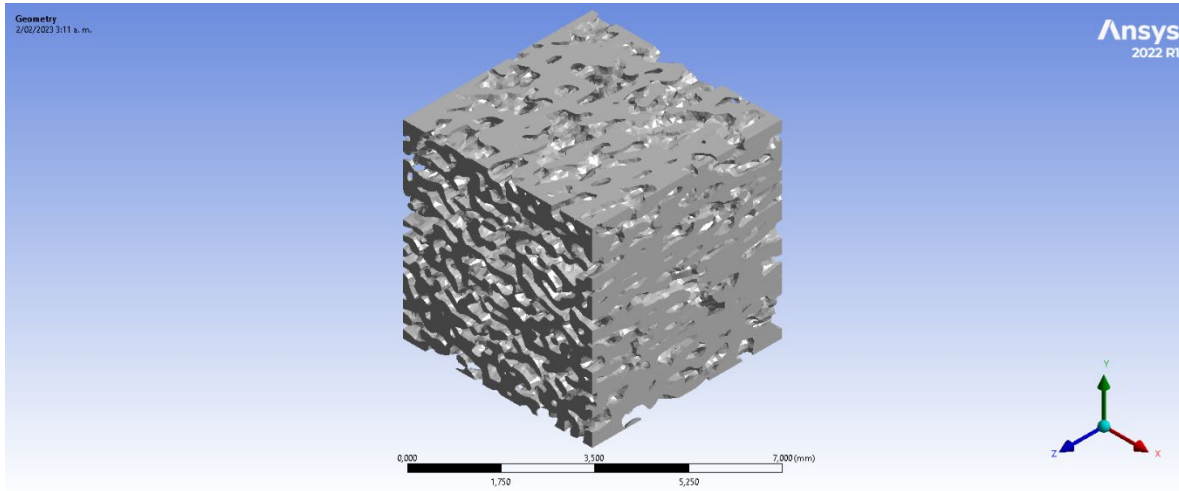


Fig. 51 Geometric model of the pig bone scaffold imported to Ansys.

The constraints and location of the axial displacement are defined, and the following model is obtained for each of the 3 main axes (Fig. 52). Finally, after the analysis, the following deformations were obtained (Fig. 53).

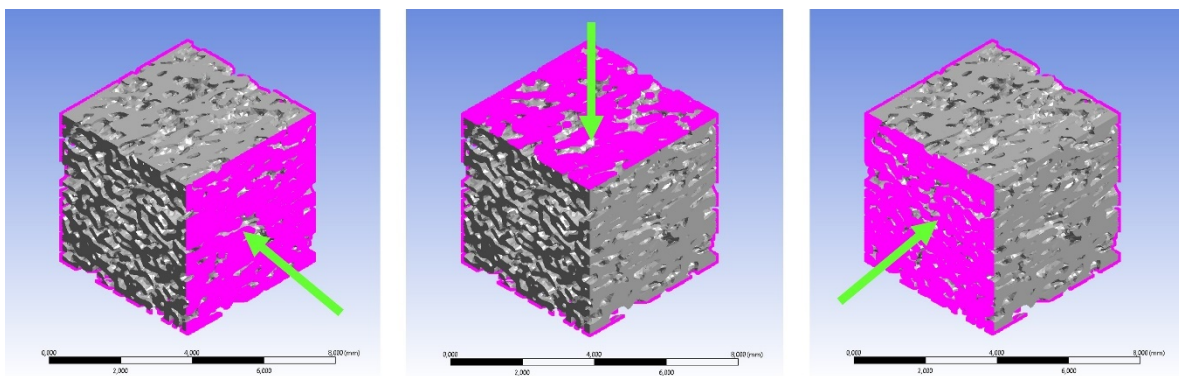


Fig. 52 Constraints and displacements for each axis. The green arrow represents the main direction of the applied displacement.

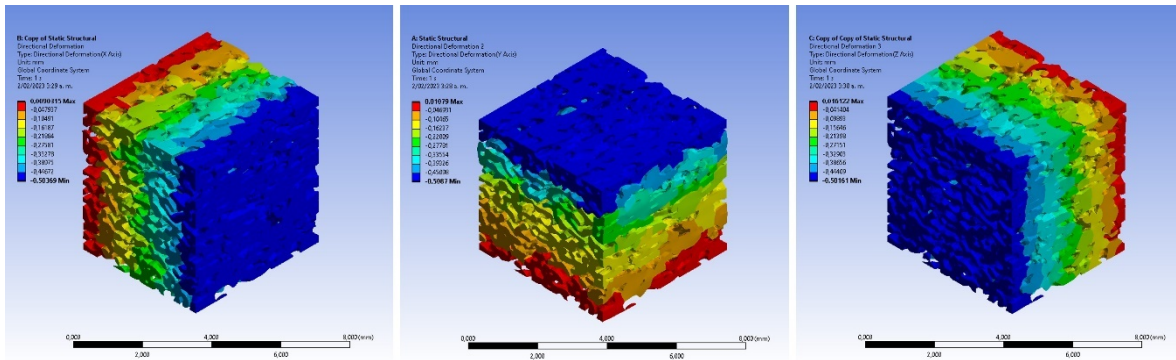


Fig. 53 Deformation results for the different displacements applied.

Table 4 Porosity and apparent Young's Modulus for the pig bone

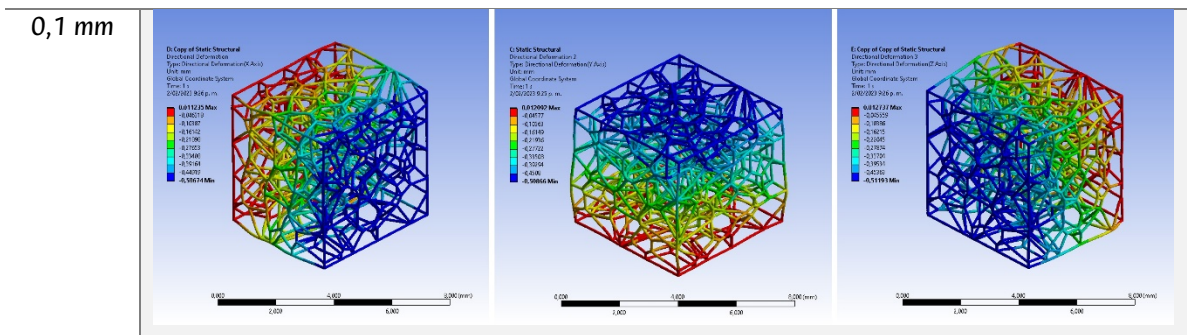
	Force (N)	Normal Stress (MPa)	Strain X	Strain Y	Strain Z	Apparent Young's Modulus (MPa)	Porosity
<b>X-Axis</b>	-319,13	-12,77	0,033868	-0,100000	0,027490	127,65	47,46%
<b>Y-Axis</b>	-136,37	-5,45	-0,100000	-0,003705	-0,006162	54,55	
<b>Z-Axis</b>	-535,78	-21,43	-0,002757	-0,003487	-0,100000	214,31	

Similarly, the percentages of porosity and apparent Young's modulus were obtained for the structures generated using the algorithm presented in section 2.2.2, and the result can be seen in Table 6. This was done to obtain Young's modulus values close to those obtained in Table 4 for pig bone. The resulting deformations for each of the corresponding trabeculae thicknesses are shown in Table 5.

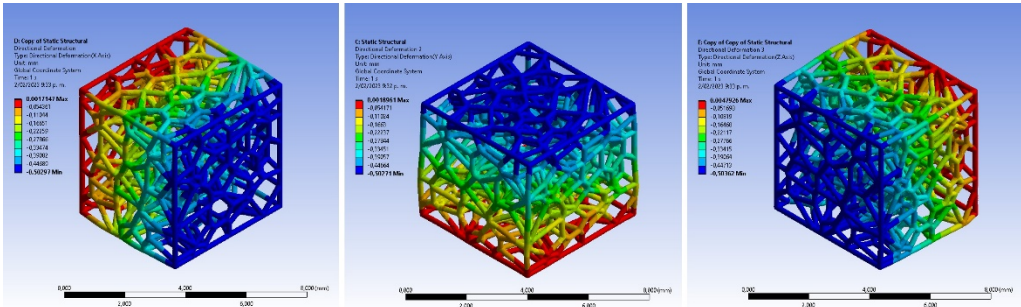
Table 5 Deformation results for the different displacements applied for each of the corresponding trabeculae thicknesses.

Trabecula width

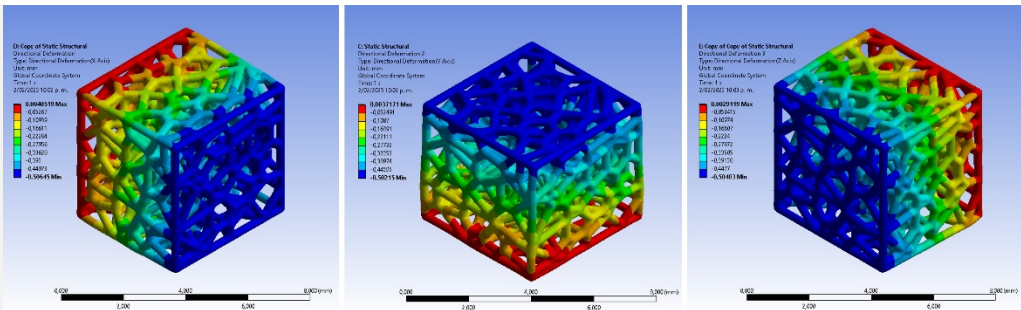
XYZ Axis Deformation



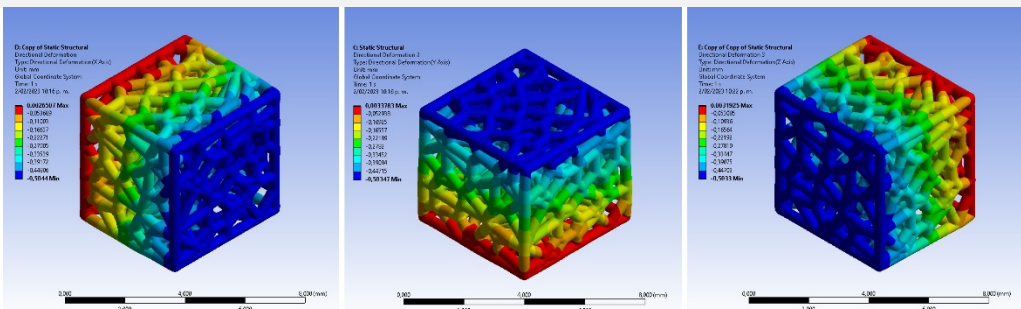
0,2 mm



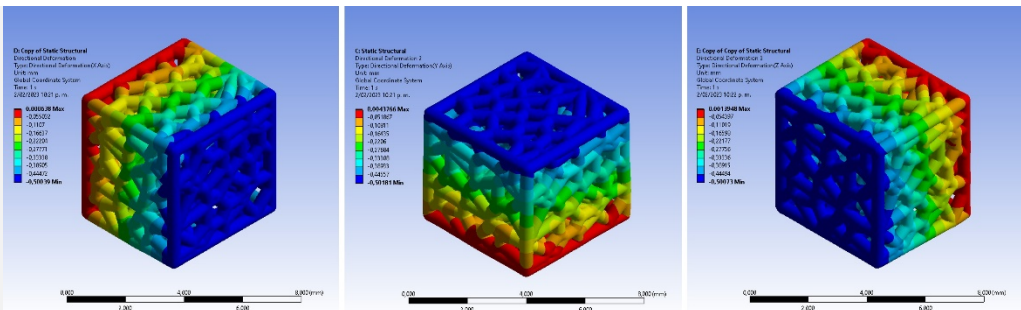
0,3 mm



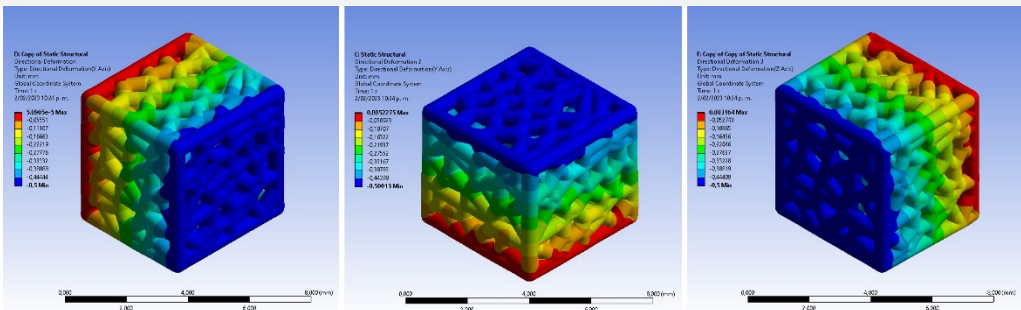
0,4 mm



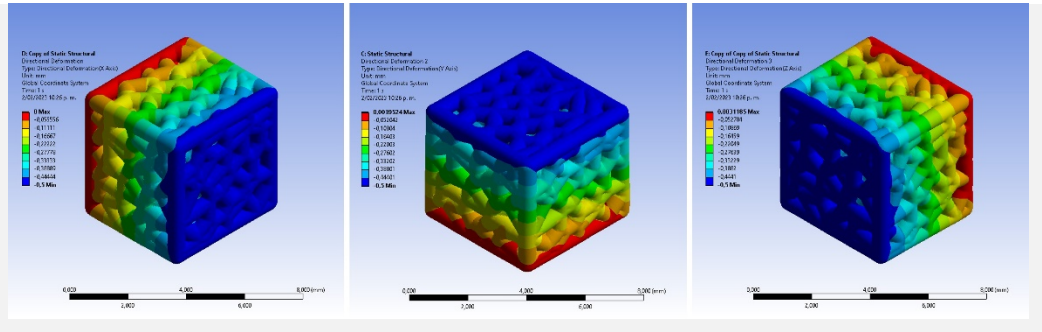
0,5 mm



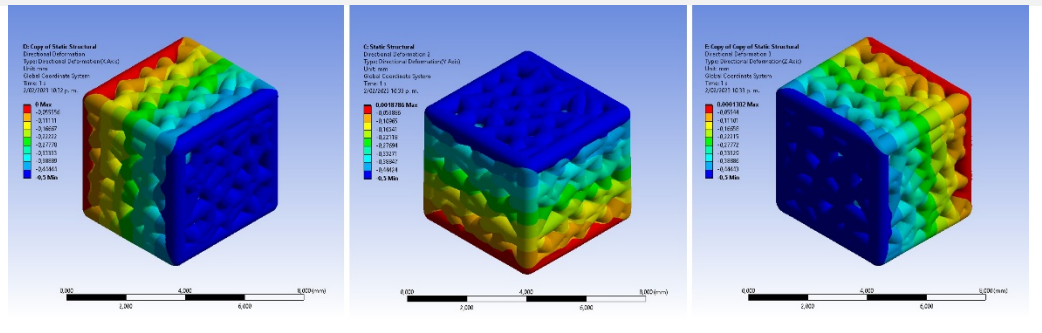
0,6 mm



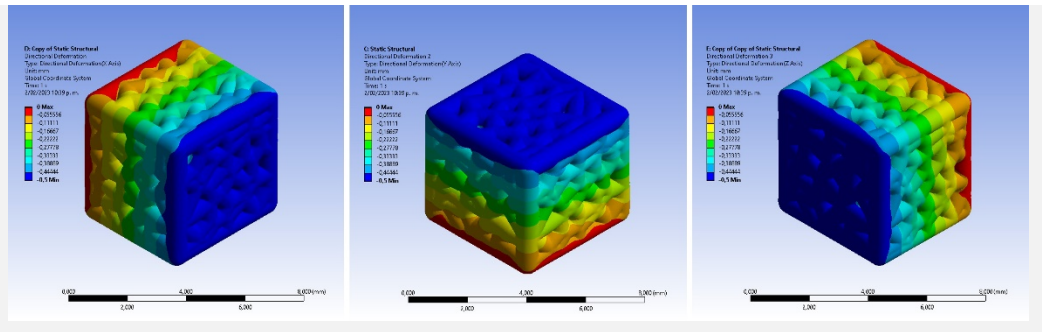
0,7 mm



0,8 mm



0,9 mm



10,0 mm

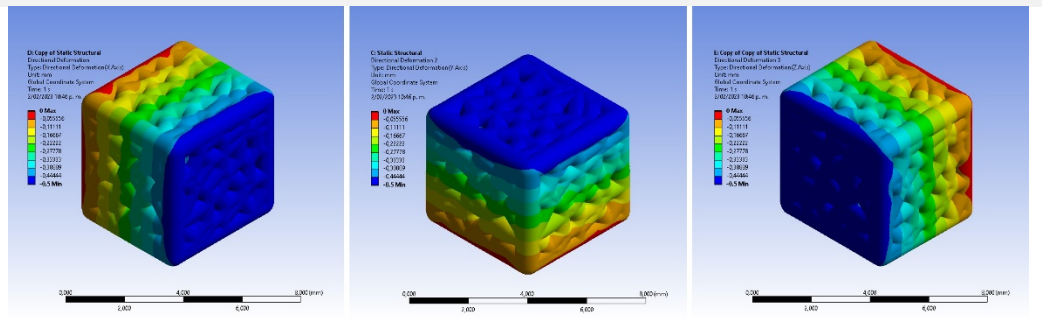




Table 6 Porosity and apparent Young's Modulus for the structures generated with the proposed algorithm increasing by 0.1 mm and alternating in the XYZ axis.

Trabecula width (mm)	Force (N)	Normal Stress (MPa)	Strain X	Strain Y	Strain Z	Apparent Young's Modulus (MPa)	Porosity
0,1 Y	-7,12	-0,28	-0,016752	-0,100000	-0,006433	2,85	95,16%
0,1 X	-7,51	-0,30	-0,100000	-0,011313	-0,010482	3,00	
0,1 Z	-7,70	-0,31	-0,020336	-0,016932	-0,100000	3,08	
0,2 Y	-48,36	-1,93	-0,008522	-0,100000	-0,004388	19,35	83,23%
0,2 X	-51,84	-2,07	-0,100000	-0,006696	-0,006170	20,74	
0,2 Z	-52,63	-2,11	-0,010333	-0,009574	-0,100000	21,05	
0,3 Y	-159,11	-6,36	-0,003287	-0,100000	-0,002446	63,64	68,00%
0,3 X	-161,41	-6,46	-0,100000	-0,003686	-0,003175	64,56	
0,3 Z	-166,24	-6,65	-0,006988	-0,004058	-0,100000	66,50	
0,4 Y	-302,90	-12,12	-0,002236	-0,100000	-0,001537	121,16	52,47%
0,4 X	-314,15	-12,57	-0,100000	-0,002918	-0,002398	125,66	
0,4 Z	-313,47	-12,54	-0,004981	-0,002828	-0,100000	125,39	
0,5 Y	-520,85	-20,83	-0,001429	-0,100000	-0,000945	208,34	38,68%
0,5 X	-534,26	-21,37	-0,100000	-0,002159	-0,002049	213,70	
0,5 Z	-529,31	-21,17	-0,003281	-0,001087	-0,100000	211,72	
0,6 Y	-732,56	-29,30	-0,001268	-0,100000	-0,001035	293,02	27,47%
0,6 X	-754,36	-30,17	-0,100000	-0,001367	-0,001655	301,74	
0,6 Z	-742,24	-29,69	-0,001920	-0,001226	-0,100000	296,90	
0,7 Y	-937,85	-37,51	0,033376	-0,100000	0,034044	375,14	19,00%
0,7 X	-964,46	-38,58	-0,100000	0,030454	0,029470	385,78	
0,7 Z	-946,05	-37,84	0,032902	0,034768	-0,100000	378,42	
0,8 Y	-1102,10	-44,08	0,033126	-0,100000	0,033600	440,84	13,20%
0,8 X	-1127,20	-45,09	-0,100000	0,030708	0,029978	450,88	
0,8 Z	-1108,20	-44,33	0,032678	0,034054	-0,100000	443,28	
0,9 Y	-1220,50	-48,82	0,034692	-0,100000	0,033900	488,20	9,58%
0,9 X	-1234,90	-49,40	-0,100000	0,030062	0,031224	493,96	
0,9 Z	-1228,10	-49,12	0,036620	0,032542	-0,100000	491,24	
1,0 Y	-1279,40	-51,18	0,033574	-0,100000	0,032868	511,76	7,56%
1,0 X	-1291,40	-51,66	-0,100000	0,029524	0,030092	516,56	
1,0 Z	-1288,80	-51,55	0,035268	0,032414	-0,100000	515,52	

Other structures and results were subsequently added to obtain values closer to those obtained for pig bone; these results can be seen in Table 7.

Table 7 Porosity and apparent Young's Modulus for the annexed structures generated with the proposed algorithm, increasing by 0.01 mm, 0.001 mm, and alternating in each axis.

Trabecula width (mm)	Force (N)	Normal Stress (MPa)	Strain X	Strain Y	Strain Z	Apparent Young's Modulus (MPa)	Porosity
<b>0,289 Y</b>	-135,35	-5,41	0,040332	-0,100000	0,037410	54,14	<b>69,77%</b>
<b>0,289 X</b>	-142,53	-5,70	-0,100000	0,033248	0,038614	57,01	
<b>0,289 Z</b>	-144,17	-5,77	0,044960	0,036196	-0,100000	57,67	
<b>0,29 Y</b>	-138,23	-5,53	0,040212	-0,100000	0,038528	55,29	<b>69,61%</b>
<b>0,29 X</b>	-145,08	-5,80	-0,100000	0,033034	0,038610	58,03	
<b>0,29 Z</b>	-147,22	-5,89	0,044106	0,034304	-0,100000	58,89	
<b>0,401 Y</b>	-316,77	-12,67	0,033966	-0,100000	0,034016	126,71	<b>52,48%</b>
<b>0,401 X</b>	-327,79	-13,11	-0,100000	0,029980	0,030246	131,12	
<b>0,401 Z</b>	-327,50	-13,10	0,034652	0,031724	-0,100000	131,00	
<b>0,41 Y</b>	-334,14	-13,37	0,034560	-0,100000	0,033370	133,66	<b>51,15%</b>
<b>0,41 X</b>	-345,42	-13,82	-0,100000	0,029696	0,031770	138,17	
<b>0,41 Z</b>	-344,62	-13,78	0,036806	0,031920	-0,100000	137,85	
<b>0,46 Y</b>	-429,31	-17,17	0,034692	-0,100000	0,033900	171,72	<b>44,05%</b>
<b>0,46 X</b>	-440,42	-17,62	-0,100000	0,030062	0,031224	176,17	
<b>0,46 Z</b>	-436,73	-17,47	0,036620	0,032542	-0,100000	174,69	
<b>0,461 Y</b>	-440,84	-17,63	0,033574	-0,100000	0,032868	176,34	<b>43,92%</b>
<b>0,461 X</b>	-451,61	-18,06	-0,100000	0,029524	0,030092	180,64	
<b>0,461 Z</b>	-447,94	-17,92	0,035268	0,032414	-0,100000	179,18	
<b>0,501 Y</b>	-529,50	-21,18	0,032940	-0,100000	0,032652	211,80	<b>38,66%</b>
<b>0,501 X</b>	-542,19	-21,69	-0,100000	0,029634	0,029784	216,88	
<b>0,501 Z</b>	-537,68	-21,51	0,034652	0,032510	-0,100000	215,07	

Once the different data were obtained for each of the structures, we selected those whose apparent Young's moduli were close to those in Table 3 and located in the same XYZ axis of this table (Table 8).

Table 8 Results of the selected structures whose values are close to those found in pig bone.

Trabeculae width (mm)	Axis	Apparent Young's Modulus for the structure (MPa)	Apparent Young's Modulus for the pig bone (MPa)	Structure's porosity	Pig bone's porosity
0,4	X	51.14	54.55	52,47%	47,46%
0,289	Y	125.66	127.65	69,77%	
0,501	Z	215.07	214.31	38,66%	

Additionally, the different porosities were also plotted with the apparent Young's modulus (Fig. 54). This graph shows how Young's modulus decreases as the percentage of porosity increases since the amount of solid material in the structure decreases. Moreover, the anisotropic behavior of the structure can be seen, and in descending order, the highest Young's modulus corresponds to the X, Z, and Y axes.

It is possible to observe how the behavior of Fig. 54 corresponds to that described by the Gibson-Ashby equation (Eq. 3) [11], [77]. This leads to a Young's modulus that exhibits a square dependence on relative density and no dependence on pore size.

$$E = Cp^n \quad \text{Eq. 3}$$

where  $E$  and  $p$  are the Young's modulus and density of the solid, respectively. The constants  $C$  and  $n$  depend on the microstructure of the solid material, and the dependence of  $C$  and  $n$  on the microstructure is not well understood, which has generated a problem in being able to predict and optimize the elastic properties of cellular solids.

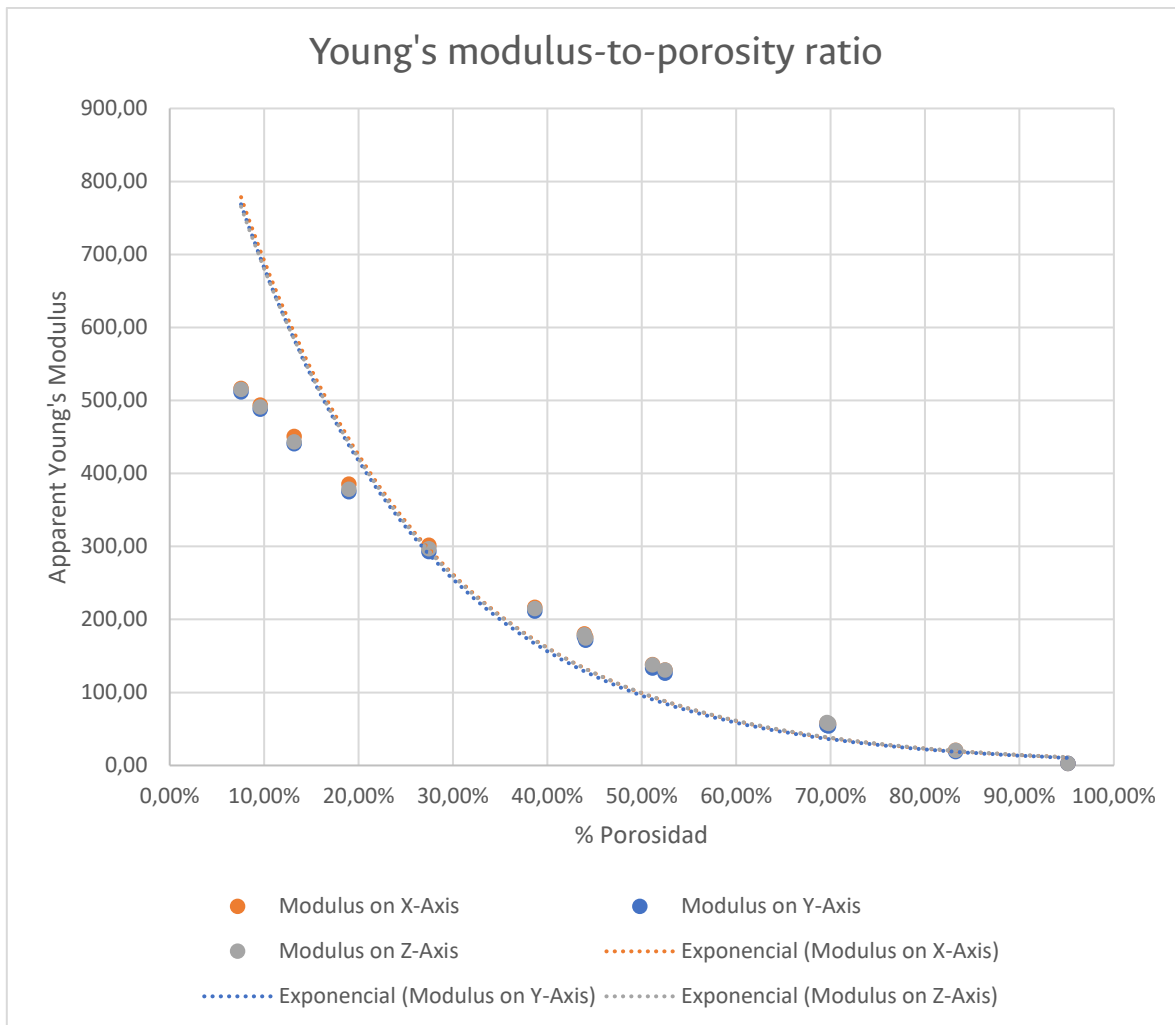


Fig. 54 The correlation of the porosity percentage with the apparent Young's modulus of the structure is shown.

### 3.2.2. Compression test

Further examination for the proposed research is carried out via compression tests on 3 cellular structures each with a different trabeculae thickness, 0.289 mm 0.4 mm and 0.501 mm (corresponding to the results shown on Table 8), and a specimen from a pig bone scan, which were manufactured by using Formlabs-2 printing system (Formlabs, Somerville, Massachusetts, USA) (Fig. 55). This system uses stereolithography technology that operates by focusing an ultraviolet (UV) laser on a container of photopolymer resin. The structures were printed on gray resin.

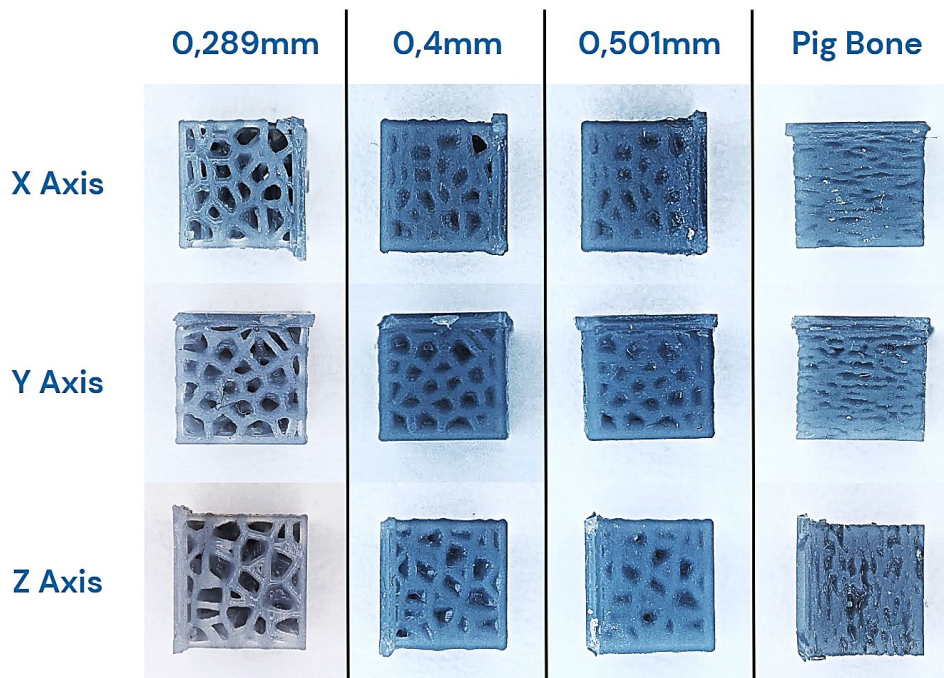


Fig. 55 3D printed structures for each trabecula thickness selected and the pig bone scan.

Four groups of structures were established to be analyzed, considering the previously selected structures, each with 3 X, Y and Z subgroups, each in turn with 3 specimens for a total of 36 specimens. Additionally, the stress–strain curve of the printing material was obtained through compression testing of solid cubes.

Before testing, the weights of each specimen were taken using a Shimadzu UW620H precision balance, and three weight measurements were taken for each structure. This was to obtain the average porosity for each structure by using the density obtained in Table 3. Additionally, dimensional measurements were obtained using a Nikon SMZ800 stereo microscope, and 5 measurements were taken for each XY, XZ, and YZ plane.



Fig. 56 Shimadzu UW620H precision balance and Nikon SMZ800 stereo microscope were used for the dimensional analysis.

The 36 specimens were subjected to a compression test in which a compression load was applied with a velocity of 0.1 mm/min. The testing apparatus used was a Shimadzu model AG-IS with a 5 kN load cell, with Trapezium 2 software (Fig. 57). The load and crosshead displacement data were recorded using the A/Data hardware and software solution produced by the same manufacturer.

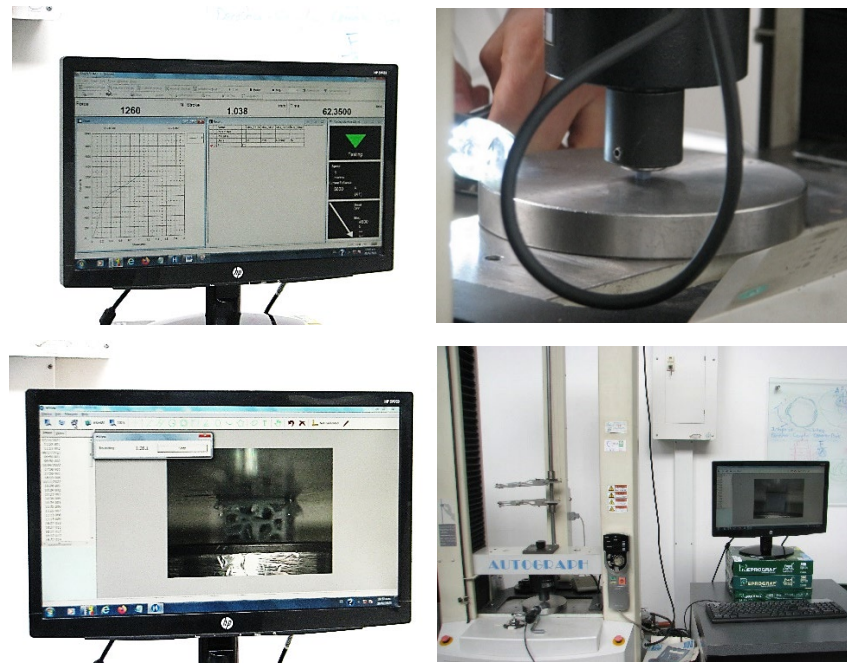


Fig. 57 Compression test setup for each specimen.

After processing and analyzing the data, Table 9 was obtained. In this table, the nominal porosities of the CAD model and the final porosity of the manufactured model can be observed, as well as the Young's modulus obtained from compression tests. Finally, a graph was made to relate the porosity and the Young's modulus obtained from the tests to better characterize the behavior of the structure.

Table 9 Results of the compression test for the selected manufactured specimens.

SPECIMEN	Nominal porosity	Real porosity	Young Modulus (MPa)		
			X Axis	Y Axis	Z Axis
<b>SOLID</b>	0%	0%	589,91	589,91	589,91
<b>PIG'S BONE</b>	47,46%	6,33%	272,69	302,55	281,71
<b>0,501 MM</b>	38,66%	10,47%	276,36	295,78	293,29
<b>0,400 MM</b>	52,47%	13,67%	282,02	233,96	187,80
<b>0,289 MM</b>	69,77%	34,00%	56,09	67,21	38,39

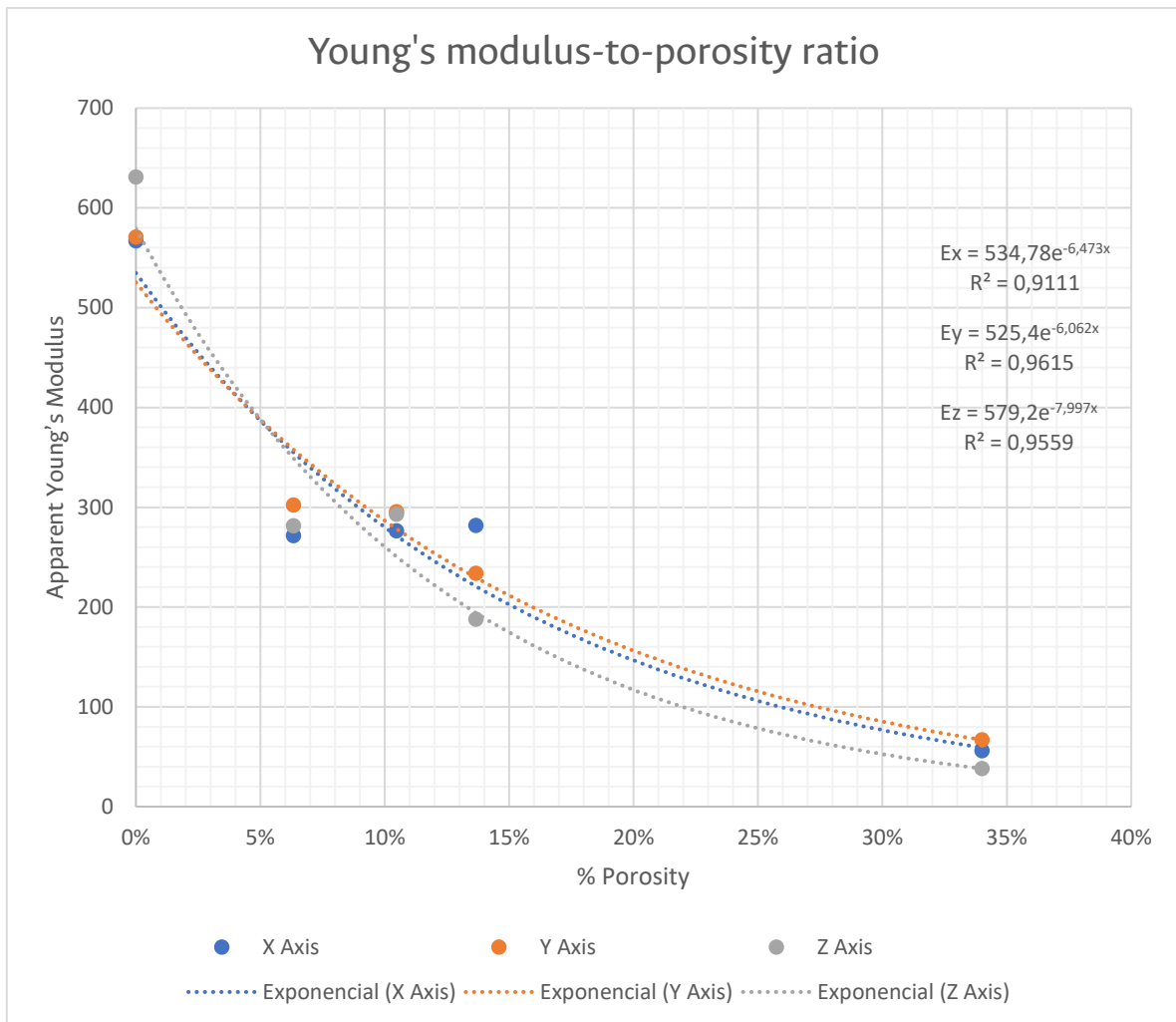


Fig. 58 The correlation of the porosity percentage with the Young's modulus of the specimens is shown.

## 4. Discussion

In this study, an algorithm was designed to generate a scaffold from computed tomography images by controlling various variables of the structure, number of pores, and trabecular size. By controlling these variables, the mechanical properties of an organic structure such as pig bone can be reproduced. The mechanical behavior observed in Fig. 54 follows that proposed by Ashby Gibson [11], and the work presented here considered the dependence of the elastic constants of Voronoi foams on the relative density [11], [78].

Moreover, the mechanical behavior observed in Fig. 58 and Table 9 shows an appreciable error regarding the real porosity of the manufactured structures versus those obtained in the CAD model. This error can be attributed to the additive manufacturing process. The 3D printed models resulted in a lower porosity because some of the pores were too small and were consequently clogged with resin, which altered the final thickness of the different trabeculae. This could modify the inertia as well as the cross-sectional area of some elements.

However, the experimental results have the same tendency as the FEA results: for greater porosity, a lesser Young's modulus. This tendency is in accordance with the model proposed by Ashby Gibson as discussed before [11].

Voronoi tessellations are used for scaffold design because their irregularity is biomimetic to the bone trabeculae [31], [79], [80]. The results showed that it is possible to obtain a synthetic Voronoi structure, customized with variable porosities and trabecular size, that can be manufactured by additive manufacturing while retaining its similarity with the natural architecture of a specific patient's bone. In addition, the interactive process of the algorithm and the use of computed tomography images facilitate the morphological adaptation process without generating mechanical complications [35].

Regarding osteogenic differentiation, the algorithm allows for the generation of porosity gradients directly related to those of bone by using CT scans as density maps. The study conducted by A. Di Luca and his collaborators showed that cells have a greater tendency toward osteogenic differentiation due to pore size due to the increased supply of nutrients and oxygen in compartments with larger pores [34].

To conclude, it should be noted that there is variability between the designed geometry and the geometry that is finally manufactured. This is because there are different processes that have variable precision:

- The export of geometry from CAD entities to an approximate representation in the STL file.
- The meshing of the STL geometry for FEM simulation.



- The SLA additive manufacturing process is conditioned by the size of the pixels and the layer thickness. Additionally, liquid resin may remain on the trabeculae, which increases the thickness of the trabeculae when the specimens are subjected to the postcuring process.

## 5. Conclusions

This thesis proposed a method for generating a three-dimensional porous structure based on Voronoi diagrams. In the second chapter of this work, various parameters for the design of 3D scaffolds are reviewed, and the concept of design through diagnostic images is introduced as a possible approach to different problems in the design of cellular materials. Among the different parameters are pore size, porosity, pore interconnectivity, mechanical properties, degradation, and biochemical signals [48]–[57], [81]. For the development of the research, those parameters directly related to the porosity and internal architecture of the cellular structure were selected. These parameters were evaluated using finite element analysis, and it was found that porosity has a direct relationship with the elastic modulus of the cellular material.

In the same chapter, the proposed methodology is used to program an algorithm that works in 2D and 3D with X-ray images and CT scans, respectively. This software uses the number of points desired and the diagnostic images as grayscale maps to represent the density distribution of the cellular structure, which results in porous structures with a density distribution that resembles that of the bone it is inspired by. Moreover, this allows the creation of a stochastic geometry that adapts to the bone's organic contours and the material's variable densities without using predefined cellular structures [82]–[84]. At this point, it is important to work the pores that are on the surface of the structure so they have a larger opening to facilitate manufacture.

Additionally, the proposed algorithm is simple to follow, offers different variables to control, unlike others found in the literature (number of point clouds, number of pores, trabeculae size, etc.), and can be applied to any geometry regardless of its complexity. Finally, the number of pores is independent of the number of pixels in the images. In addition, thanks to the use of density maps in diagnostic images, the final structure does not depend directly on the number of pixels or voxels in the images.

In the third chapter, the mechanical compression behavior of the structures generated through finite element analysis and mechanical testing of specimens manufactured by additive manufacturing was characterized. It was found that it is necessary to consider the effect of postprocessing in the manufacturing process to achieve printed cellular structures closer to the initially designed CAD structure, especially in terms of porosity.

It is important to mention that due to the process that the CAD models must go through during design, analysis, and subsequent manufacturing, tolerance errors may occur that can affect the mechanical and dimensional behavior of the final structures. This process includes designing the 3D CAD model using Grasshopper and Rhinoceros 3D, translating the CAD to meshing for finite elements using Gmesh and Ansys Workbench, and then transferring it to the STL extension for manufacturing using 3D printing. Finally, during the development of the chapter, it can be observed how the elastic modulus can be adjusted by varying the thickness of the trabeculae; however, further studies are necessary to adjust the elasticity modulus in each of the axes and subsequently the transverse elasticity modulus.

### 5.1. Products

- As part of this work, there is one article in process of publication with the title “*Design for the additive manufacturing of structural elements with cellular materials using Voronoi diagrams and Delaunay triangulations: Biological and structural applications*”.
- A software code was registered in the “Dirección nacional de derechos de autor”: Scaffold regular. Registration number 13-92-296. Date: Nov 8th, 2022.

### 5.2. Future work

The chapters in this thesis provide a foundation for exploring specific applications and conducting further research. Some of the points that can be addressed are related to the following:

- The roughness of the final surface of the structure was changed to analyze and improve cell adhesion, and initial work in this field can be seen in Fig. 59.
- Generate a greater anisotropy in the mechanical properties of the principal axes to more faithfully emulate the mechanical behavior of cellular structures in regard to bones or other organic structures.
- Conduct experimental studies to establish the effect of the manufacturing and postprocessing on the final dimensions and mechanical behavior of the designed structures.



Fig. 59 possible surface roughness proposed.

## References

- [1] M. A. Velasco, C. A. Narvaez-Tovar, and D. A. Garzon-Alvarado, "Design, materials, and mechanobiology of biodegradable scaffolds for bone tissue engineering.," *Biomed Res Int*, vol. 2015, p. 729076, 2015, doi: 10.1155/2015/729076.
- [2] J. A. Buckwalter, M. J. Glimcher, R. R. Cooper, and R. Recker, "Bone biology. I: Structure, blood supply, cells, matrix, and mineralization.," *Instr Course Lect*, vol. 45, pp. 371–86, 1996, doi: 10.3390/jfb1010022.
- [3] J. F. A. Barreto, "Regeneración ósea a través de la ingeniería de tejidos : una introducción Osseous Regeneration through Tissue Engineering :," *Redalyc.org*, p. 13, 2009, [Online]. Available: <http://www.redalyc.org/pdf/1792/179214945008.pdf>
- [4] K. a Hing, "Bone repair in the twenty-first century: biology, chemistry or engineering?," *Philos Trans A Math Phys Eng Sci*, vol. 362, no. 1825, pp. 2821–50, 2004, doi: 10.1098/rsta.2004.1466.
- [5] International Osteoporosis Foundation, "Osteoporosis en Colombia," *International Osteoporosis Foundation*, p. 3, 2012, [Online]. Available: [https://www.iofbonehealth.org/sites/default/files/media/PDFs/Regional Audits/2012-Latin\\_America\\_Audit-Colombia-ES\\_0\\_0.pdf](https://www.iofbonehealth.org/sites/default/files/media/PDFs/Regional_Audits/2012-Latin_America_Audit-Colombia-ES_0_0.pdf)
- [6] Elespectador.com, "En Colombia se realizan 10.000 reemplazos de cadera o rodilla al año - ELESPECTADOR.COM," *El Espectador*, Bogotá, 2009. Accessed: Nov. 25, 2019. [Online]. Available: <https://www.elespectador.com/noticias/salud/articulo114216-colombia-se-realizan-10000-reemplazos-de-cadera-o-rodilla-al-ano>
- [7] N. Ospina Vélez, "Reemplazo articular aumenta en personas jóvenes," *El Colombiano*, 2012. Accessed: Nov. 25, 2019. [Online]. Available: [https://www.elcolombiano.com/historico/reemplazo\\_articular\\_aumenta\\_en\\_personas\\_jovenes-EBEC\\_177333](https://www.elcolombiano.com/historico/reemplazo_articular_aumenta_en_personas_jovenes-EBEC_177333)
- [8] D. Z. Amaro, "Regeneración de tejido : Una solución para la deficiencia ósea," 2012.
- [9] L. J. Bonassar and C. a Vacanti, "Tissue engineering: the first decade and beyond.," *J Cell Biochem Suppl*, vol. 30–31, no. September, pp. 297–303, 1998, doi: 10.1002/(SICI)1097-4644(1998)72.

- [10] W. M. Saltzman and T. R. Kyriakides, *Cell interactions with polymers\_Lanza19.pdf*, Third Edit. Elsevier Inc., 2014. doi: 10.1016/B978-0-12-370615-7.50024-X.
- [11] L. J. Gibson and M. F. Ashby, *Cellular Solids*, vol. 22, no. 4. Cambridge: Cambridge University Press, 1997. doi: 10.1017/CBO9781139878326.
- [12] M. Scheffler and P. Colombo, *Cellular Ceramics*. Wiley, 2005. doi: 10.1002/3527606696.
- [13] L. J. Gibson, M. F. Ashby, G. N. Karam, U. Wegst, and H. R. Shercliff, "The Mechanical Properties of Natural Materials. II. Microstructures for Mechanical Efficiency," *Proceedings: Mathematical and Physical Sciences*, vol. 450. Royal Society, pp. 141–162. doi: 10.2307/52663.
- [14] J. G. Skedros and S. L. Baucom, "Mathematical analysis of trabecular 'trajectories' in apparent trajectorial structures: the unfortunate historical emphasis on the human proximal femur," *J Theor Biol*, vol. 244, no. 1, pp. 15–45, Jan. 2007, doi: 10.1016/j.jtbi.2006.06.029.
- [15] C. H. Turner, "On Wolff's law of trabecular architecture," *J Biomech*, vol. 25, no. 1, pp. 1–9, Jan. 1992, doi: 10.1016/0021-9290(92)90240-2.
- [16] L. Esteban-Tejeda *et al.*, "Bone tissue scaffolds based on antimicrobial SiO<sub>2</sub>-Na<sub>2</sub>O-Al<sub>2</sub>O<sub>3</sub>-CaO-B<sub>2</sub>O<sub>3</sub> glass," *J Non Cryst Solids*, vol. 432, pp. 73–80, 2016, doi: 10.1016/j.jnoncrysol.2015.05.040.
- [17] Q. Fu, *Bioactive Glass Scaffolds for Bone Tissue Engineering*. Elsevier Ltd., 2019. doi: 10.1016/b978-0-08-102196-5.00015-x.
- [18] Y. Kim, J. Y. Lim, G. H. Yang, J.-H. Seo, H.-S. Ryu, and G. Kim, "3D-printed PCL/bioglass (BGS-7) composite scaffolds with high toughness and cell-responses for bone tissue regeneration," *Journal of Industrial and Engineering Chemistry*, 2019, doi: 10.1016/j.jiec.2019.06.027.
- [19] Z. Khurshid *et al.*, *Novel Techniques of Scaffold Fabrication for Bioactive Glasses*. Elsevier Ltd., 2019. doi: 10.1016/b978-0-08-102196-5.00018-5.
- [20] A. M. Deliormanli, "Size-dependent degradation and bioactivity of borate bioactive glass," *Ceram Int*, vol. 39, no. 7, pp. 8087–8095, 2013, doi: 10.1016/j.ceramint.2013.03.081.

- [21] J. Wieding, A. Wolf, and R. Bader, "Numerical optimization of open-porous bone scaffold structures to match the elastic properties of human cortical bone," *J Mech Behav Biomed Mater*, vol. 37, pp. 56–68, 2014, doi: 10.1016/j.jmbbm.2014.05.002.
- [22] D. W. Rosen, S. Johnston, M. Reed, and H. Wang, "Design of General Lattice Structures for Lightweight and Compliance Applications," *Rapid Manufacturing Conference*, no. March, pp. 1–14, 2006.
- [23] S. M. Giannitelli, D. Accoto, M. Trombetta, and A. Rainer, "Current trends in the design of scaffolds for computer-aided tissue engineering," *Acta Biomater*, vol. 10, no. 2, pp. 580–594, 2014, doi: 10.1016/j.actbio.2013.10.024.
- [24] M. A. Wettergreen, B. S. Bucklen, B. Starly, E. Yuksel, W. Sun, and M. A. K. Liebschner, "Creation of a unit block library of architectures for use in assembled scaffold engineering," *Computer-Aided Design*, vol. 37, no. 11, pp. 1141–1149, Sep. 2005, doi: DOI: 10.1016/j.cad.2005.02.005.
- [25] C. K. Chua, K. F. Leong, C. M. Cheah, and S. W. Chua, "Development of a Tissue Engineering Scaffold Structure Library for Rapid Prototyping . Part 2 : Parametric Library and Assembly Program," *Advanced manufacturing technology*, vol. 21, pp. 302–312, 2003.
- [26] Y. Wang, "Periodic surface modeling for computer aided nano design," *CAD Computer Aided Design*, vol. 39, no. 3, pp. 179–189, Mar. 2007, doi: 10.1016/j.cad.2006.09.005.
- [27] I. Maskery *et al.*, "Insights into the mechanical properties of several triply periodic minimal surface lattice structures made by polymer additive manufacturing," *Polymer (Guildf)*, vol. 152, pp. 62–71, Sep. 2018, doi: 10.1016/J.POLYMER.2017.11.049.
- [28] O. Sigmund and K. Maute, "Topology optimization approaches," *Structural and Multidisciplinary Optimization*, vol. 48, no. 6, pp. 1031–1055, Dec. 2013, doi: 10.1007/s00158-013-0978-6.
- [29] J. Wang and R. Rai, "Classification of Bio-Inspired Periodic Cubic Cellular Materials Based on Compressive Deformation Behaviors of 3D Printed Parts and FE Simulations," in *Volume 7: 28th International Conference on Design Theory and Methodology*, ASME, Aug. 2016, p. V007T06A003. doi: 10.1115/DETC2016-59729.
- [30] S. J. Hollister, R. A. Levy, T.-M. Chu, J. W. Halloran, and S. E. Feinberg, "An image-based approach for designing and manufacturing craniofacial scaffolds," *Int J Oral Maxillofac Surg*, vol. 29, no. 1, pp. 67–71, 2000, doi: 10.1034/j.1399-0020.2000.290115.x.

- [31] M. Fantini and M. Curto, "Interactive design and manufacturing of a Voronoi-based biomimetic bone scaffold for morphological characterization," *International Journal on Interactive Design and Manufacturing (IJDeM)*, vol. 12, no. 2, pp. 585–596, May 2018, doi: 10.1007/s12008-017-0416-x.
- [32] S. Krish and Sivam, "A practical generative design method," *Computer-Aided Design*, vol. 43, no. 1, pp. 88–100, Jan. 2011, doi: 10.1016/j.cad.2010.09.009.
- [33] G. Marchiori *et al.*, "Design of a novel procedure for the optimization of the mechanical performances of 3D printed scaffolds for bone tissue engineering combining CAD, Taguchi method and FEA," *Med Eng Phys*, vol. 69, pp. 92–99, 2019, doi: 10.1016/j.medengphy.2019.04.009.
- [34] A. Di Luca *et al.*, "Gradients in pore size enhance the osteogenic differentiation of human mesenchymal stromal cells in three-dimensional scaffolds," *Sci Rep*, vol. 6, no. February, pp. 1–13, 2016, doi: 10.1038/srep22898.
- [35] G. Staffa *et al.*, "Custom made bioceramic implants in complex and large cranial reconstruction: A two-year follow-up," *Journal of Cranio-Maxillofacial Surgery*, vol. 40, no. 3, 2012, doi: 10.1016/j.jcms.2011.04.014.
- [36] A. R. Smith, "Alpha and the history of digital compositing," *Microsoft Tech Memo 7*, vol. 24, pp. 1–10, 1995.
- [37] D.-S. Kim and K. Sugihara, "New trends in Voronoi diagrams for CAD/CAM/CAE," *Computer-Aided Design*, vol. 41, no. 5, pp. 325–326, May 2009, doi: 10.1016/J.CAD.2008.10.001.
- [38] S. Fortune, "Voronoi diagrams and delaunay triangulations," in *Handbook of Discrete and Computational Geometry, Third Edition*, 2017, pp. 705–721. doi: 10.1201/9781315119601.
- [39] Fred A. Mettler.r., *Essentials of Radiology*, vol. 1. 2005. doi: 10.1136/bmj.1.4647.229-a.
- [40] S. Bose, M. Roy, and A. Bandyopadhyay, "Recent advances in bone tissue engineering scaffolds," *Trends Biotechnol*, vol. 30, no. 10, pp. 546–554, Oct. 2012, doi: 10.1016/j.tibtech.2012.07.005.
- [41] J. P. Bilezikian, L. G. Raisz, and T. J. Martin, *Principles of Bone Biology 3*, vol. 1, no. 9. Academic Press, 2008. doi: 10.3174/ajnr.A1712.

- [42] D. Alfredo and Q. Rodríguez, "MODELO COMPUTACIONAL DE REMODELAMIENTO ÓSEO MEDIANTE ESTRUCTURAS DISCRETAS," Universidad Nacional de Colombia, Bogotá, 2021.
- [43] M. P. Bendsøe and O. Sigmund, *Topology Optimization*. Berlin, Heidelberg: Springer Berlin Heidelberg, 2004. doi: 10.1007/978-3-662-05086-6.
- [44] M. P. Bendsøe, "Optimal shape design as a material distribution problem," *Structural Optimization*, vol. 1, no. 4, pp. 193–202, 1989, doi: 10.1007/BF01650949.
- [45] M. Yliperttula, B. G. Chung, A. Navaladi, A. Manbachi, and A. Urtili, "High-throughput screening of cell responses to biomaterials," *European Journal of Pharmaceutical Sciences*, vol. 35, no. 3, pp. 151–160, Oct. 02, 2008. doi: 10.1016/j.ejps.2008.04.012.
- [46] R. Dimitriou, E. Jones, D. McGonagle, and P. v Giannoudis, "Bone regeneration: current concepts and future directions," *BMC Med*, vol. 9, no. 1, p. 66, Dec. 2011, doi: 10.1186/1741-7015-9-66.
- [47] V. Karageorgiou and D. Kaplan, "Porosity of 3D biomaterial scaffolds and osteogenesis," *Biomaterials*, vol. 26, no. 27, pp. 5474–5491, 2005, doi: 10.1016/j.biomaterials.2005.02.002.
- [48] S. Hofmann *et al.*, "Control of in vitro tissue-engineered bone-like structures using human mesenchymal stem cells and porous silk scaffolds," *Biomaterials*, vol. 28, no. 6, pp. 1152–1162, Feb. 2007, doi: 10.1016/j.biomaterials.2006.10.019.
- [49] A. C. Jones, C. H. Arns, D. W. Hutmacher, B. K. Milthorpe, A. P. Sheppard, and M. A. Knackstedt, "The correlation of pore morphology, interconnectivity and physical properties of 3D ceramic scaffolds with bone ingrowth," *Biomaterials*, vol. 30, no. 7, pp. 1440–1451, Mar. 2009, doi: 10.1016/j.biomaterials.2008.10.056.
- [50] Y. Wang, U. J. Kim, D. J. Blasioli, H. J. Kim, and D. L. Kaplan, "In vitro cartilage tissue engineering with 3D porous aqueous-derived silk scaffolds and mesenchymal stem cells," *Biomaterials*, vol. 26, no. 34, pp. 7082–7094, Dec. 2005, doi: 10.1016/j.biomaterials.2005.05.022.
- [51] L. Meinel *et al.*, "Engineering bone-like tissue in vitro using human bone marrow stem cells and silk scaffolds," *J Biomed Mater Res A*, vol. 71, no. 1, pp. 25–34, Oct. 2004, doi: 10.1002/jbm.a.30117.

- [52] L. Meinel *et al.*, "Silk implants for the healing of critical size bone defects," *Bone*, vol. 37, no. 5, pp. 688–698, 2005, doi: 10.1016/j.bone.2005.06.010.
- [53] L. Meinel *et al.*, "Engineering cartilage-like tissue using human mesenchymal stem cells and silk protein scaffolds," *Biotechnol Bioeng*, vol. 88, no. 3, pp. 379–391, Nov. 2004, doi: 10.1002/bit.20252.
- [54] L. Uebersax *et al.*, "Effect of Scaffold Design on Bone Morphology In Vitro."
- [55] X. Liu and P. X. Ma, "Polymeric Scaffolds for Bone Tissue Engineering," 2004.
- [56] W. L. Murphy, R. G. Dennis, J. L. Kileny, and D. J. Mooney, "Salt Fusion: An Approach to Improve Pore Interconnectivity within Tissue Engineering Scaffolds," 2002.
- [57] K. J. L. Burg, S. Porter, and J. F. Kellam, "Biomaterial developments for bone tissue engineering," *Biomaterials*, vol. 21, no. 23, pp. 2347–2359, 2000, doi: 10.1016/S0142-9612(00)00102-2.
- [58] D. W. Hutmacher, "Scaffolds in tissue engineering bone and cartilage," 2000.
- [59] J. Raghunath, J. Rollo, K. M. Sales, P. E. Butler, and A. M. Seifalian, "Biomaterials and scaffold design: key to tissue-engineering cartilage," *Biotechnol Appl Biochem*, vol. 46, no. 2, p. 73, Feb. 2007, doi: 10.1042/ba20060134.
- [60] K. Rezwani, Q. Z. Chen, J. J. Blaker, and A. R. Boccaccini, "Biodegradable and bioactive porous polymer/inorganic composite scaffolds for bone tissue engineering," *Biomaterials*, vol. 27, no. 18, pp. 3413–3431, Jun. 2006. doi: 10.1016/j.biomaterials.2006.01.039.
- [61] Y. Wang, H. J. Kim, G. Vunjak-Novakovic, and D. L. Kaplan, "Stem cell-based tissue engineering with silk biomaterials," *Biomaterials*, vol. 27, no. 36, pp. 6064–6082, Dec. 2006. doi: 10.1016/j.biomaterials.2006.07.008.
- [62] C. Vepari and D. L. Kaplan, "Silk as a biomaterial," *Progress in Polymer Science (Oxford)*, vol. 32, no. 8–9, pp. 991–1007, Aug. 2007. doi: 10.1016/j.progpolymsci.2007.05.013.
- [63] Y. Wang *et al.*, "In vivo degradation of three-dimensional silk fibroin scaffolds," *Biomaterials*, vol. 29, no. 24–25, pp. 3415–3428, Aug. 2008, doi: 10.1016/j.biomaterials.2008.05.002.
- [64] L. S. Nair and C. T. Laurencin, "Biodegradable polymers as biomaterials," *Progress in Polymer Science (Oxford)*, vol. 32, no. 8–9, pp. 762–798, Aug. 2007. doi: 10.1016/j.progpolymsci.2007.05.017.



- [65] E. Dawson, G. Mapili, K. Erickson, S. Taqvi, and K. Roy, "Biomaterials for stem cell differentiation," *Advanced Drug Delivery Reviews*, vol. 60, no. 2. pp. 215–228, Jan. 14, 2008. doi: 10.1016/j.addr.2007.08.037.
- [66] C. A. Gersbach, J. E. Phillips, and A. J. García, "Genetic engineering for skeletal regenerative medicine," *Annual Review of Biomedical Engineering*, vol. 9. pp. 87–119, 2007. doi: 10.1146/annurev.bioeng.9.060906.151949.
- [67] S. Cartmell, "Controlled release scaffolds for bone tissue engineering," *J Pharm Sci*, vol. 98, no. 2, pp. 430–441, 2009, doi: 10.1002/jps.21431.
- [68] F. Ben-Hatira, K. Saidane, and A. Mrabet, "A finite element modeling of the human lumbar unit including the spinal cord," *J Biomed Sci Eng*, vol. 05, no. 03, pp. 146–152, 2012, doi: 10.4236/jbise.2012.53019.
- [69] F. A. Pintar N Yoganandan M Pesigan J Reinartz A Sances and J. J. F Cusick, "Cervical Vertebral Strain Measurements Under Axial and Eccentric Loading," 1995. [Online]. Available: <http://biomechanical.asmedigitalcollection.asme.org/>
- [70] M. P. Lutolf and J. A. Hubbell, "Synthetic biomaterials as instructive extracellular microenvironments for morphogenesis in tissue engineering," *Nat Biotechnol*, vol. 23, no. 1, pp. 47–55, 2005.
- [71] B. D. Boyan, T. W. Hummert, D. D. Dean, and Z. Schwartz, "Role of material surfaces in regulating bone and cartilage cell response," *Biomaterials*, vol. 17, no. 2, pp. 137–146, 1996.
- [72] B. A. C. Harley, H.-D. Kim, M. H. Zaman, I. V Yannas, D. A. Lauffenburger, and L. J. Gibson, "Microarchitecture of three-dimensional scaffolds influences cell migration behavior via junction interactions," *Biophys J*, vol. 95, no. 8, p. 4013–4024, 2008, doi: 10.1529/biophysj.107.122598.
- [73] S.-W. Choi, Y. Zhang, M. R. Macewan, and Y. Xia, "Neovascularization in biodegradable inverse opal scaffolds with uniform and precisely controlled pore sizes," *Adv Healthc Mater*, vol. 2, no. 1, p. 145–154, 2013, doi: 10.1002/adhm.201200106.
- [74] S. J. Hollister, "Porous scaffold design for tissue engineering," vol. 4, no. July, 2005.
- [75] L. R. Madden *et al.*, "Proangiogenic scaffolds as functional templates for cardiac tissue engineering," *Proc Natl Acad Sci U S A*, vol. 107, no. 34, p. 15211–15216, 2010, doi: 10.1073/pnas.1006442107.

- [76] F. Bai *et al.*, “The effect of pore size on tissue ingrowth and neovascularization in porous bioceramics of controlled architecture in vivo Biomed.” *Mater*, 2011.
- [77] A. P. Roberts and E. J. Garboczi, “ELASTIC MODULI OF MODEL RANDOM THREE-DIMENSIONAL CLOSED-CELL CELLULAR SOLIDS,” 2001. [Online]. Available: [www.elsevier.com/locate/actamat](http://www.elsevier.com/locate/actamat)
- [78] Y. X. Gan, C. Chen, and Y. P. Shen, “Three-dimensional modeling of the mechanical property of linearly elastic open cell foams,” *Int J Solids Struct*, vol. 42, no. 26, pp. 6628–6642, Dec. 2005, doi: 10.1016/j.ijsolstr.2005.03.002.
- [79] B. Herath *et al.*, “Mechanical and geometrical study of 3D printed Voronoi scaffold design for large bone defects,” *Mater Des*, vol. 212, p. 110224, 2021, doi: 10.1016/j.matdes.2021.110224.
- [80] S. Gómez, M. D. Vlad, J. López, and E. Fernández, “Design and properties of 3D scaffolds for bone tissue engineering,” *Acta Biomater*, vol. 42, no. June, pp. 341–350, 2016, doi: 10.1016/j.actbio.2016.06.032.
- [81] V. Karageorgiou and D. Kaplan, “Porosity of 3D biomaterial scaffolds and osteogenesis,” *Biomaterials*, vol. 26, no. 27. Elsevier BV, pp. 5474–5491, 2005. doi: 10.1016/j.biomaterials.2005.02.002.
- [82] C. K. Chua, K. F. Leong, C. M. Cheah, and S. W. Chua, “Development of a Tissue Engineering Scaffold Structure Library for Rapid Prototyping . Part 2 : Parametric Library and Assembly Program,” *Advanced manufacturing technology*, vol. 21, pp. 302–312, 2003.
- [83] N. Chantarapanich, P. Puttawibul, S. Sucharitpawatskul, P. Jeamwattanachai, S. Inglam, and K. Sitthiseripratip, “Scaffold Library for Tissue Engineering: A Geometric Evaluation,” vol. 2012, 2012, doi: 10.1155/2012/407805.
- [84] M. A. Wettergreen, B. S. Bucklen, B. Starly, E. Yuksel, W. Sun, and M. A. K. Liebschner, “Creation of a unit block library of architectures for use in assembled scaffold engineering,” *Computer-Aided Design*, vol. 37, no. 11, pp. 1141–1149, Sep. 2005, doi: DOI: 10.1016/j.cad.2005.02.005.